

SKYRMIONS IN MAGNETIC MATERIALS



Krishnan Ganesh & Harvey Marples

Supervisor: Dr. Kevin Edmonds
Department of Physics & Astronomy
University of Nottingham

A thesis submitted in partial fulfilment
of the requirements for the degree:

Masters in Science

26th May 2021

Abstract

This thesis investigates the collective excitations of magnetic skyrmions and their instabilities using a micromagnetic simulation developed in Python. Our simulation numerically integrates the Landau-Lifshitz-Gilbert equation for a lattice of magnetic spins. Through the application of an out-of-plane magnetic pulse, we excite a radial breathing mode of a single skyrmion, whose resonant frequency increases with magnetic field strength. Excitation by an in-plane magnetic pulse results in a counter-clockwise rotational mode of the skyrmion core. We analyse our numerical results using scaling relations and toy-models based on the continuum theory. We also identify elliptical and quadrupolar instabilities of the skyrmion, occurring for certain values of the magnetic field. By numerically diagonalising the Landau-Lifshitz-Gilbert equation, we investigate the possibility that these instabilities arise due to gapless magnon modes of the skyrmion, but find that the lowest energy magnon modes remain gapped for all magnetic fields. By modelling the deformation as the insertion of a helical domain wall between two half-skyrmions, we are able to analytically approximate the critical field for the elliptical instability.

Contents

Introduction	3
1 Theory of Magnetic Skyrmions	4
1.1 The Dzyaloshinskii-Moriya interaction	4
1.2 Continuum theory	5
1.2.1 Helical phase for $Z = 0$	5
1.2.2 Skyrmion solution for $Z > 0$	6
1.3 Topological properties	8
1.4 The Landau-Lifshitz-Gilbert Equation	9
1.5 Collective Coordinates	11
2 Simulation Method	13
2.1 System Model	13
2.2 System of Units	14
2.3 Developing the Simulation	15
2.4 Single skyrmion initial condition	16
2.5 Topological charge on a lattice	17
2.6 Decay Into Helical, SkX, or Ferromagnetic State	18
3 Pulsed Dynamics	21
3.1 Out-of-Plane Pulses	21
3.2 In-Plane Pulses	24
3.3 Missing resonances and Skyrmion Mass	26
3.4 Summary	29
4 Instabilities and Magnon modes	30
4.1 Geometric Instabilities	30
4.2 The magnon problem	31
4.3 Bound Magnon modes	33
4.4 Energetic considerations	36
4.5 Summary	37
5 Discussion & Outlook	39
5.1 Performance Issues and Optimisation	39
5.2 Theoretical Limitations	40
5.3 Next Nearest Neighbour Interactions	40
5.4 Bi-meron wires	41
Conclusion	43
Bibliography	44

Introduction

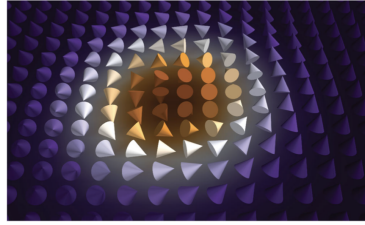


Figure 1: Illustration of skyrmion spin-texture, reproduced from [1]

In 1961, Tony Skyrme proposed a model that envisioned nucleons to be swirling patterns in the pion field, characterised by a single integer called a *winding number*: a so-called "skyrmion" [2][3]. Whilst Nature chooses to build her nucleons out of quarks rather than swirling patterns, the skyrmion model has recently enjoyed a spectacular resurgence in the field of condensed matter physics.

Remarkably, in certain non-centrosymmetric magnetic materials, skyrmions manifest themselves as swirling spin textures that are localised in the ferromagnetic phase (Figure 1). These vortices exhibit a variety of rich physics such as emergent gauge fields, skyrmion Hall effects and skyrmion breathing modes [4][5][6].

Since their experimental observation in crystals such as MnSi and Cu₂OSeO₃ [7][8], magnetic skyrmions have attracted the attention of the spintronics research community. One compelling prospect is to use skyrmions as a novel form of data storage. Since skyrmion winding numbers are invariant under continuous deformations, bits encoded in these winding numbers are topologically protected. Furthermore, their propensity for transport by ultra-low current density [9] and small size, could mean future skyrmionic devices consume less energy and offer higher information density than conventional ferromagnetic memory.

In recent years, it has become evident that magnetic skyrmions are not purely particle-like, rigid entities. These vortices can ripple and vibrate when perturbed by microwave magnetic fields [10][11][12]. Therefore, investigating their dynamic deformation properties is crucial for assessing their viability as information carriers. In this thesis, we investigate the collective excitations of magnetic skyrmions and their instabilities. Chapter 1 will lay down the theoretical tools used in the study of magnetic skyrmions. This will be followed by a detailed exposition of our micromagnetic simulation method in Chapter 2. Chapter 3 will detail our studies of the collective excitations of a single skyrmion using an AC magnetic pulse. In Chapter 4, we identify elliptical and quadrupolar instabilities of the skyrmion and investigate the possibility of these instabilities originating from gapless magnon modes. Finally, Chapter 5 states the limitations of our numerical and analytical calculations, before discussing directions for future research.

Chapter 1

Theory of Magnetic Skyrmions

In this section, we outline the important physical concepts and analytical tools used in the study of magnetic skyrmions. Many of the intuitions presented in this chapter are drawn upon in later investigations to discuss numerical findings.

1.1 The Dzyaloshinskii-Moriya interaction

A cornerstone of nanoscale magnetism is the Heisenberg Hamiltonian [13]:

$$\mathcal{H}_{Heis} = \sum_{\mathbf{r}} \sum_{j=\{x,y\}} -J \mathbf{n}_{\mathbf{r}} \cdot \mathbf{n}_{\mathbf{r}+a\hat{\mathbf{e}}_j} - Z \hat{\mathbf{e}}_z \cdot \mathbf{n}_{\mathbf{r}} \quad (1.1.1)$$

This Hamiltonian captures two effects: nearest-neighbour exchange coupling between spins $\mathbf{n}_{\mathbf{r}}$ with coupling strength J , and Zeeman coupling of spins to an external magnetic field aligned along the z -axis, with coupling strength Z ¹. In this thesis, $|\mathbf{n}_{\mathbf{r}}| = 1$ and is treated as a classical vector. Since the exchange interaction favours colinear spins, and the Zeeman interaction favours spins to be aligned with the z -axis, this model cannot admit swirling spin textures such as skyrmions.

For the existence of skyrmions, we require the Dzyaloshinskii-Moriya (DM) interaction:

$$\mathcal{H}_{DM} = D \sum_{\mathbf{r}} \hat{\mathbf{e}}_x \cdot (\mathbf{n}_{\mathbf{r}} \times \mathbf{n}_{\mathbf{r}+a\hat{\mathbf{e}}_x}) + \hat{\mathbf{e}}_y \cdot (\mathbf{n}_{\mathbf{r}} \times \mathbf{n}_{\mathbf{r}+a\hat{\mathbf{e}}_y}) \quad (1.1.2)$$

Physically, this coupling can arise in *non-centrosymmetric* crystals, when the interactions between neighbouring spins are mediated by a non-magnetic atom with strong spin-orbit coupling. A combination of the exchange interaction with spin-orbit coupling physics can produce an effective DM interaction [14][15]. Common examples of such crystals include MnSi and Cu₂OSeO₃. Equation 1.1.2 is a specific case of the more general form [16]:

$$\mathcal{H}_{DM,general} = \sum_{\mathbf{r}} \sum_{j=\{x,y\}} (\tilde{D} \hat{\mathbf{e}}_j) \cdot (\mathbf{n}_{\mathbf{r}} \times \mathbf{n}_{\mathbf{r}+a\hat{\mathbf{e}}_j}) \quad (1.1.3)$$

where \tilde{D} is the 2×2 DM tensor whose form depends on the symmetry properties of the underlying crystal lattice. For the case of Equation 1.1.2:

$$\tilde{D} = \begin{pmatrix} D & 0 \\ 0 & D \end{pmatrix}$$

¹ a is the lattice constant.

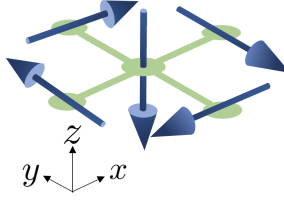


Figure 1.1: For a simple 5-site model, the DMI interaction stabilises a vortex-like spin configuration.

Due to the cross product structure of Equation 1.1.3, this interaction favours orthogonal neighbouring spins. For a simple 5-site model, it is trivial to show that Equation 1.1.2 is minimised for the vortex-like spin configuration shown in Figure 1.1. This is because the energy of each bond is $-D$. Upon including the exchange interaction, we would expect the spins to wind over many unit cells. Furthermore, the effect of Zeeman coupling would be to favour the number of up-spins in the system, thus *localising* the vortex. These arguments provide a physical intuition for why skyrmions may form in lattices described by the full Hamiltonian:

$$\mathcal{H} = \mathcal{H}_{Heis} + \mathcal{H}_{DM} \quad (1.1.4)$$

Solving for the ground state of Equation 1.1.4, for a lattice of many spins, necessitates a micromagnetic simulation approach, which will be discussed in Chapter 2

1.2 Continuum theory

The ersatz intuition of the previous section can be analytically justified if we take the continuum limit of the Hamiltonian ($a \rightarrow 0$) [17]:

$$\mathcal{H} = \int d^2\mathbf{r} \frac{J}{2} \sum_{i=\{x,y\}} (\partial_i \mathbf{n})^2 + D \mathbf{n} \cdot (\nabla \times \mathbf{n}) + Z(1 - n_z) \quad (1.2.1)$$

where $\mathbf{n}(\mathbf{r})$ is now a continuous spin field. To ensure that the ferromagnetic state has zero energy, we have added a constant energy shift to the Zeeman term. For many systems, the continuum limit is justified, since spin textures often span several unit cells. We now outline two important cases:

1.2.1 Helical phase for $Z = 0$

The zero field case can be solved using the Fourier transformed spin field [1]:

$$\mathbf{n}(\mathbf{r}) = \sum_{\mathbf{k}} \mathbf{n}_{\mathbf{k}} e^{i\mathbf{k}\cdot\mathbf{r}} \quad (1.2.2)$$

where $\mathbf{n}_{\mathbf{k}} = \mathbf{n}_{-\mathbf{k}}^*$. Plugging this into Equation 1.2.1 and integrating over space we get:

$$\mathcal{H} = \sum_{\mathbf{k}} \frac{J}{2} |\mathbf{k}|^2 \mathbf{n}_{\mathbf{k}} \cdot \mathbf{n}_{-\mathbf{k}} + iD\mathbf{k} \cdot (\mathbf{n}_{\mathbf{k}} \times \mathbf{n}_{-\mathbf{k}}) \quad (1.2.3)$$

Importantly, the DM term is minimised when the mode amplitudes $\mathbf{n}_{\mathbf{k}}$ and $\mathbf{n}_{-\mathbf{k}}$ are both orthogonal to the wave-vector \mathbf{k} . Physically, this corresponds to a phase where the

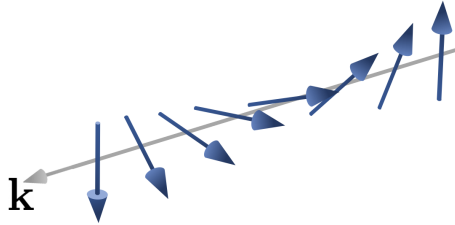


Figure 1.2: In the absence of an external magnetic field, the helical phase is stabilised, with wave-vector of spin-spiral \mathbf{k} .

spins wind *helically* along the wave-vector \mathbf{k} , as shown in Figure 1.2. To calculate the wavelength of this helix, one can decompose \mathbf{n}_k into its real and imaginary parts:

$$\mathbf{n}_k = \mathbf{u}_k + i\mathbf{v}_k$$

which gives:

$$\mathcal{H} = \sum_{\mathbf{k}} \frac{J}{2} |\mathbf{k}|^2 (|\mathbf{u}_k|^2 + |\mathbf{v}_k|^2) + 2D\mathbf{k} \cdot (\mathbf{u}_k \times \mathbf{v}_k) \quad (1.2.4)$$

Taking $|\mathbf{u}_k| = |\mathbf{v}_k|$, and minimising w.r.t $|\mathbf{k}|$, the optimal wavenumber is:

$$|\mathbf{k}| = \frac{D}{J} \quad (1.2.5)$$

Therefore, localised magnetic skyrmions *cannot* be stabilised for zero magnetic field.

1.2.2 Skyrmion solution for $Z > 0$

To solve the full Hamiltonian, we must take a more general approach by expressing the spin field in spherical polars:

$$\mathbf{n}(\mathbf{r}) = \sin \Theta \cos \Phi \hat{\mathbf{e}}_x + \sin \Theta \sin \Phi \hat{\mathbf{e}}_y + \cos \Theta \hat{\mathbf{e}}_z \quad (1.2.6)$$

where Θ and Φ are position dependent. Motivated by the swirling pattern of the skyrmion in Figure 1, we look for solutions where:

$$\Theta = \Theta(r) \quad \text{and} \quad \Phi = \varphi + \pi/2$$

with $\{r, \varphi\}$ being the radial coordinate and azimuthal angle respectively. Upon substituting this into Equation 1.2.1 and integrating over φ , one obtains:

$$\frac{\mathcal{H}}{2\pi J} = \int_0^\infty \rho d\rho \left[\underbrace{\frac{1}{2}(\partial_\rho \Theta)^2 + \frac{\sin^2(\Theta)}{2\rho^2}}_{\text{Exchange}} + \underbrace{\partial_\rho \Theta + \frac{\sin(2\Theta)}{2\rho}}_{\text{DM}} + \underbrace{\frac{ZJ}{D^2}(1 - \cos \Theta)}_{\text{Zeeman}} \right] \quad (1.2.7)$$

where we have re-scaled r in the following way:

$$\rho = \frac{D}{J} r \quad (1.2.8)$$

A detailed derivation can be found in references: [17] [18].

From Equation 1.2.7, we see that the problem boils down to calculating the function $\Theta(\rho)$ such that \mathcal{H} is minimised. This is a calculus of variations problem, with Euler-Lagrange equation:

$$\partial_\rho^2 \Theta + \frac{1}{\rho} \partial_\rho \Theta - \frac{\sin 2\Theta}{2\rho^2} + \frac{2 \sin^2 \Theta}{\rho} - \frac{ZJ}{D^2} \sin \Theta = 0 \quad (1.2.9)$$

This differential equation must be solved for specific values of Z , J and D , subject to appropriate boundary conditions. Since we are looking for localised skyrmion solutions, far away from the centre of the skyrmion ($\rho \rightarrow \infty$), we expect the spins to be aligned with the z -axis. Therefore, the central spin must be inverted. These considerations warrant the following boundary conditions:

$$\Theta(\rho = 0) = \pi \quad \text{and} \quad \Theta(\rho \rightarrow \infty) = 0 \quad (1.2.10)$$

Exact solutions that satisfy these boundary conditions are best obtained by numerical methods. Before discussing these, we choose to study the asymptotics of $\Theta(\rho)$.

In the limit $\rho \rightarrow 0$, we expect the function to decrease linearly from π :

$$\Theta(\rho) \approx \pi - C \frac{D}{J} r \quad (1.2.11)$$

where C is a numerical constant. For large distances from the origin, the small-angle approximation $\sin \Theta \approx \Theta$ can be utilised to obtain the differential equation:

$$\rho^2 \partial_\rho^2 \Theta + \rho \partial_\rho \Theta - \frac{ZJ}{D^2} \rho^2 \Theta = 0 \quad (1.2.12)$$

This is the modified Bessel differential equation [19], resulting in the asymptotic solution:

$$\Theta(\rho) \sim \mathcal{K}_0 \left(\sqrt{\frac{Z}{J}} r \right) \quad (1.2.13)$$

where \mathcal{K}_0 is the modified Bessel function of the second kind. These functions resemble an exponential decay for large r . Importantly, this tells us that the system admits finite-sized skyrmion solutions for finite magnetic field. The corresponding “decay length” l is ²:

$$l = \sqrt{J/Z}$$

This is the characteristic length scale over which spins re-orient to align with the ferromagnetic phase. For larger Z (effectively a larger magnetic field), the decay length decreases. This appeals to our physical intuition which says for high Zeeman coupling, there is a greater energy penalty associated with the spins smoothly winding into the ferromagnetic phase. Therefore, for high magnetic fields, we expect a sharp boundary between the edge of the skyrmion and the ferromagnetic phase.

Figure 1.3 shows a numerically obtained plot of the skyrmion energy $\mathcal{H}/2\pi J$ against ZJ/D^2 . Furthermore, the inset shows solutions for $\Theta(\rho)$ corresponding to $ZJ/D^2 = 0.7$ and $ZJ/D^2 = 1.5$. In order to solve Equation 1.2.9, we used the shooting method as described in [20]. This involves supplying an initial condition $\{\pi, \partial_\rho \Theta(0)\}$, that is numerically integrated up to a maximum value of ρ_{max} .

²Sometimes also called the “healing length” or “magnetic screening length”

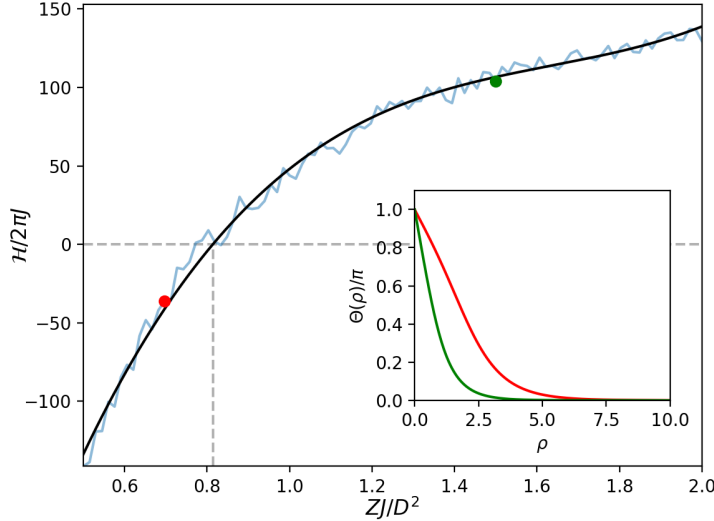


Figure 1.3: Total energy of skyrmion $\mathcal{H}/2\pi J$ against interaction constant ZJ/D^2 (blue). A line of best fit has been plotted to guide the eye (black). **Inset:** Numerical solutions for skyrmion profile $\Theta(\rho)$ represented by the red and green dots.

Next, an interval bisection routine is used to change the value of $\partial_\rho \Theta(0)$ based on whether $\Theta(\rho_{max})$ overshoots or undershoots 0. This process is repeated until the solution meets the aforementioned boundary conditions. A similar plot can be found in [21].

From Figure 1.3 we see that the single skyrmion solution is a positive energy, meta-stable excitation in the ferromagnetic phase for $ZJ/D^2 \gtrsim 0.8$. Furthermore, the solutions for $\Theta(\rho)$ show that the size of the skyrmion core decreases for increasing Z . For sufficiently high Z , one can expect the skyrmion to collapse, leaving only the ferromagnetic phase.

For $ZJ/D^2 \lesssim 0.8$, the system favours the creation of skyrmions since the total energy is negative. This can result in the proliferation of skyrmion textures, leading to the formation of a skyrmion lattice [7].

1.3 Topological properties

A curious feature of magnetic skyrmions is that they possess a non-zero topological charge (or winding number). In the continuum limit, this is mathematically defined by:

$$\mathcal{Q} = \frac{1}{4\pi} \int dx dy \mathbf{n} \cdot (\partial_x \mathbf{n} \times \partial_y \mathbf{n}) \quad (1.3.1)$$

Since 4π is the total solid angle of a sphere, this quantity counts the number of times the spins “wrap” the unit sphere.

A useful way to visualise this concept is by stereo-graphic projection of spins onto the unit sphere (\mathbb{P}). This is schematically illustrated in Figure 1.4. A line is drawn between the spin and the “north pole” of the unit sphere. The spin is projected onto the point where the line intersects the surface of the sphere. Naturally, points at infinity will be projected on the north-pole. In this way, one can cover the sphere with spins and study the number of times the spin vectors wrap the unit sphere.

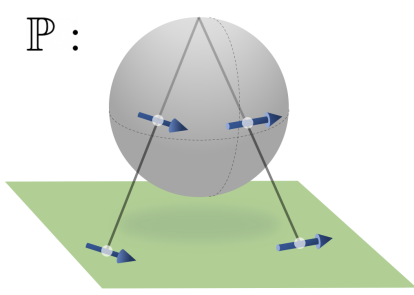


Figure 1.4: Stereographic projection of spins onto the unit sphere.

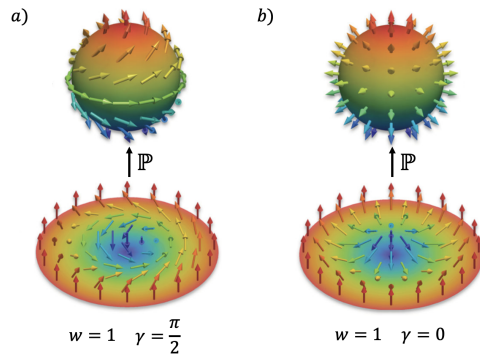


Figure 1.5: Stereographic projections of (a) Bloch and (b) Neél skyrmions. Images adapted from [1].

The previous section studied a skyrmion whose spins wrapped in a vortex-like fashion, given by the azimuthal angle:

$$\Phi(\varphi) = \varphi + \pi/2$$

This configuration is called a *Bloch* skyrmion because cuts across the diameter of the skyrmion reveal Bloch domain walls. The corresponding stereographic projection is shown in Figure 1.5(a). However, in principle one could consider a more general expression:

$$\Phi(\varphi) = w\varphi + \gamma \quad (1.3.2)$$

For $w = 1$ and $\gamma = 0$, a Neél skyrmion is obtained, as shown in Figure 1.5(b).

By studying Figures 1.5(a) and 1.5(b), one can deduce that the two spin textures are related by a global phase rotation. Topology enters the discussion when we evaluate the topological charge integral for the two spin-textures, yielding:

$$Q = w = +1$$

for *both* spin textures. Even-though the Bloch and Neél skyrmion are geometrically inequivalent, they are topologically equivalent since they possess the same winding number. The main distinction between Bloch and Neél skyrmions is an energetic one, since they are stabilised by different forms of the DM tensor. In fact, for any smooth, continuous deformation of the skyrmion, the topological charge remains invariant. As stated in the introduction, this feature of skyrmionic textures makes them novel candidates for information storage.

1.4 The Landau-Lifshitz-Gilbert Equation

In order to study the dynamics of magnetic skyrmions, one needs an equation of motion for the spins. This is given by the semi-classical Landau-Lifshitz-Gilbert (LLG) equation [22]:

$$\frac{\partial \mathbf{n}(\mathbf{r}, t)}{\partial t} = \frac{\gamma}{N} \mathbf{H}_{eff} \times \mathbf{n} + \alpha \mathbf{n} \times \frac{\partial \mathbf{n}}{\partial t} \quad (1.4.1)$$

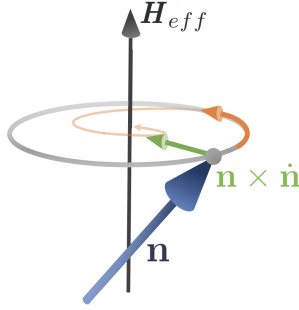


Figure 1.6: Diagram of vectors involved in the Landau-Lifshitz-Gilbert equation.

where \mathcal{N} is the magnitude of the dipole moment produced by the spin, and γ is the usual gyro-magnetic ratio³. The first term on the right hand side describes precession of the spins about an effective magnetic field \mathbf{H}_{eff} . This field stems from the local interactions present in the Hamiltonian (Equation 1.2.1), and is given by:

$$\mathbf{H}_{eff} = -\frac{\delta \mathcal{H}}{\delta \mathbf{n}} \quad (1.4.2)$$

where $\frac{\delta}{\delta \mathbf{n}}$ denotes the functional derivative w.r.t \mathbf{n} . Using integration by parts on the exchange interaction term, one finds:

$$\mathbf{H}_{eff} = \frac{J}{2} \nabla^2 \mathbf{n} - D(\nabla \times \mathbf{n}) + Z \hat{\mathbf{e}}_z \quad (1.4.3)$$

The Laplacian implies that the exchange interaction has an averaging effect on the spins. In addition, the curl term implies that the DM induced magnetic field is stronger in regions of higher vorticity, further reflecting its propensity for stabilising swirling spin textures. The Zeeman term is trivially constant everywhere in the sample.

The second term on the right hand side of Equation 1.4.1 corresponds to damping of this precession, which eventually causes the spins to reach a steady state. α is the dimensionless Gilbert damping constant [23]. This is a phenomenological damping parameter which captures the effects of dissipative processes, such as collisions with phonons and eddy currents. For realistic materials, $\alpha \sim 10^{-2}$. These details are illustrated in Figure 1.6.

By expanding the cross products, and regrouping the $\partial \mathbf{n} / \partial t$ terms, one can rewrite Equation 1.4.1 in inverted form:

$$\frac{\partial \mathbf{n}}{\partial t} = -\frac{\gamma/\mathcal{N}}{1+\alpha^2} [\mathbf{n} \times \mathbf{H}_{eff} + \alpha \mathbf{n} \times (\mathbf{n} \times \mathbf{H}_{eff})] \quad (1.4.4)$$

Equation 1.4.4 has the advantage that the time derivative appears on the left hand side only, making it easier to integrate numerically. Numerical solutions to the LLG equations will be the subject of Chapter 2.

³Technically, this is a dynamical equation for the magnetic dipole moments. Our terminology will freely switch between magnetic moments and spins, since the two are simply related by a proportionality factor.

1.5 Collective Coordinates

The LLG equation describes a system of many spins interacting with each-other via local nearest neighbour interactions. Thus, exact analytical solutions only exist for the simplest of cases. The intractable nature of the problem stems from the fact that the spin vector field $\mathbf{n}[\mathbf{r}, t]$ has infinite degrees of freedom. However, progress can be made by approximating the dynamics to only depend on a finite set of collective coordinates $\xi(t)$:

$$\xi(t) = \{\xi_1(t), \xi_2(t), \dots, \xi_n(t)\}$$

so that:

$$\mathbf{n}[\mathbf{r}, t] \approx \mathbf{n}[\mathbf{r}, \xi(t)]$$

Physically, this approximation is warranted if there are only a few degrees of freedom that are negligibly damped, whilst all others rapidly approach their steady-state values [24]. For instance, if the dynamics only consists of rigid translations of the skyrmion, a sensible choice would be $\xi(t) = \{X(t), Y(t)\}$, where $X(t)$ and $Y(t)$ are coordinates of the centre of the skyrmion. For such a choice of collective coordinates, the spin vector field can be approximated by $\mathbf{n}[\mathbf{r} - X(t)\hat{\mathbf{e}}_x - Y(t)\hat{\mathbf{e}}_y]$, which is of the travelling wave form.

The virtue of the collective coordinate formalism, is that one can derive effective equations of motion for $\xi(t)$. This is achieved by re-expressing the time-derivative $\partial\mathbf{n}/\partial t$ in the LLG equation using chain-rule:

$$\frac{\partial\mathbf{n}}{\partial t} \approx \sum_{i=1}^n \frac{\partial\mathbf{n}}{\partial\xi_i} \dot{\xi}_i(t) \quad (1.5.1)$$

Substituting this into Equation 1.4.1 and integrating over space, we obtain:

$$\sum_{i=1}^n \int d^2\mathbf{r} \frac{\partial\mathbf{n}}{\partial\xi_i} \dot{\xi}_i(t) = \sum_{i=1}^n \int d^2\mathbf{r} \mathbf{n} \times \left\{ \frac{\gamma}{\mathcal{N}} \frac{\delta\mathcal{H}}{\delta\mathbf{n}} + \alpha \frac{\partial\mathbf{n}}{\partial\xi_i} \dot{\xi}_i(t) \right\} \quad (1.5.2)$$

Taking the cross product of both sides with \mathbf{n} , and using the vector identity:

$$\mathbf{a} \times (\mathbf{b} \times \mathbf{c}) = (\mathbf{a} \cdot \mathbf{c})\mathbf{b} - (\mathbf{a} \cdot \mathbf{b})\mathbf{c}$$

One can obtain equations of motion in ξ_i :

$$\sum_{j=1}^n G_{ij}\xi_j - \Gamma_{ij}\xi_j - \frac{\partial\mathcal{H}}{\partial\xi_i} = 0 \quad (1.5.3)$$

where G_{ij} is the gyrotropic tensor given by:

$$G_{ij} = \frac{\mathcal{N}}{\gamma} \int d^2\mathbf{r} \mathbf{n} \cdot \left(\frac{\partial\mathbf{n}}{\partial\xi_i} \times \frac{\partial\mathbf{n}}{\partial\xi_j} \right) \quad (1.5.4)$$

and Γ_{ij} is the dissipative matrix:

$$\Gamma_{ij} = \frac{\alpha\mathcal{N}}{\gamma} \int d^2\mathbf{r} \frac{\partial\mathbf{n}}{\partial\xi_i} \cdot \frac{\partial\mathbf{n}}{\partial\xi_j} \quad (1.5.5)$$

Equation 1.5.3 can also be envisioned as the Euler-Lagrange equation to an effective Lagrangian \mathcal{L} [25]:

$$\mathcal{L} = \mathbf{A} \cdot \dot{\boldsymbol{\xi}} - \mathcal{H}[\boldsymbol{\xi}] \quad (1.5.6)$$

where the gauge field \mathbf{A} is related to the gyrotropic tensor by:

$$G_{ij} = \frac{\partial A_j}{\partial \xi_i} - \frac{\partial A_i}{\partial \xi_j} \quad (1.5.7)$$

The Lagrangian definition of Equation 1.5.6 will be used in the study of rotational modes in Chapter 3.

Chapter 2

Simulation Method

In this chapter, we describe the steps taken to develop a fully functioning micro-magnetic simulation. We also validate our simulation for a few simple scenarios that are routinely reported in the literature.

2.1 System Model

In our 2D system, we consider a square lattice of $N \times N$ atomic sites with lattice constant a . The system is described by the Hamiltonian:

$$\mathcal{H} = \sum_{\mathbf{r}} \sum_{k=\{x,y\}} -J \mathbf{n}_{\mathbf{r}} \cdot \mathbf{n}_{\mathbf{r}+a\hat{\mathbf{e}}_k} - Z \hat{\mathbf{b}} \cdot \mathbf{n}_{\mathbf{r}} + (\tilde{D} \hat{\mathbf{e}}_k) \cdot (\mathbf{n}_{\mathbf{r}} \times \mathbf{n}_{\mathbf{r}+a\hat{\mathbf{e}}_k}) \quad (2.1.1)$$

where the first term describes the exchange interaction between neighbouring spins with exchange stiffness J . The second term corresponds to the Zeeman coupling of spins to an external magnetic field with Zeeman coupling strength Z , defined by the unit vector $\hat{\mathbf{b}}$. The final term corresponds to the generalised DM interaction, described by the DM tensor \tilde{D} .

Each lattice site is denoted by two indices $\{i, j\}$, with the indexing scheme illustrated in Figure 2.1. The magnetic moment at lattice site $\{i, j\}$ evolves according to the Landau-Lifshitz-Gilbert (LLG) equation

$$\frac{\partial \mathbf{n}_{i,j}}{\partial t} = -\frac{\gamma/\mathcal{N}}{1+\alpha^2} [\mathbf{n}_{i,j} \times \mathbf{H}_{i,j}^{eff} + \alpha \mathbf{n}_{i,j} \times (\mathbf{n}_{i,j} \times \mathbf{H}_{i,j}^{eff})] \quad (2.1.2)$$

where the effective magnetic field at lattice site $\{i, j\}$ is given by:

$$\mathbf{H}_{i,j}^{eff} = -\frac{\partial \mathcal{H}}{\partial \mathbf{n}_{i,j}}$$

Note that in the discrete theory, the functional derivative of Equation 1.4.2 has been replaced by a partial derivative, which can be evaluated by hand for the various interactions in the Hamiltonian.

The exchange contribution to the effective magnetic field is:

$$\mathbf{H}_{i,j}^{Exch} = J(\mathbf{n}_{i+1,j} + \mathbf{n}_{i-1,j} + \mathbf{n}_{i,j+1} + \mathbf{n}_{i,j-1}) \quad (2.1.3)$$

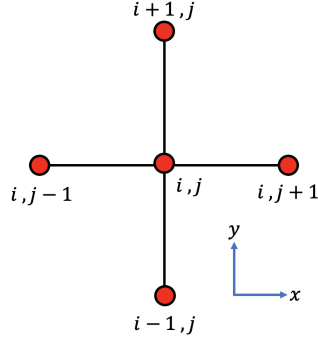


Figure 2.1: Indexing scheme for lattice sites.

This expression implies that the exchange interaction generates an effective field that is proportional to the average spin of the neighbouring sites. This is to be expected, since the exchange interaction favours neighbouring spins to be aligned. Upon differentiating the Zeeman term, we obtain:

$$\mathbf{H}_{i,j}^{Zee} = Z\hat{\mathbf{b}} \quad (2.1.4)$$

The Zeeman contribution is relatively simple as the external magnetic field is uniform, hence the effective field at each lattice site is equal. For the majority of this thesis we will take $\hat{\mathbf{b}} = \hat{\mathbf{e}}_z$.

For DM tensor $\tilde{D} = D\mathbb{1}$:

$$\mathcal{H}_{DM} = D \sum_{i,j} (\mathbf{n}_{i,j} \times \mathbf{n}_{i+1,j}) \cdot \hat{\mathbf{e}}_x + (\mathbf{n}_{i,j} \times \mathbf{n}_{i,j+1}) \cdot \hat{\mathbf{e}}_y \quad (2.1.5)$$

which gives rise to the effective field:

$$\mathbf{H}_{i,j}^{DMI} = D \{ (n_{i,j+1}^z - n_{i,j-1}^z) \hat{\mathbf{e}}_x - (n_{i+1,j}^z - n_{i-1,j}^z) \hat{\mathbf{e}}_y + (n_{i+1,j}^y - n_{i-1,j}^y - n_{i,j+1}^x + n_{i,j-1}^x) \hat{\mathbf{e}}_z \} \quad (2.1.6)$$

where n^x , n^y and n^z are the magnetisation vector components. Equation 2.1.6 is precisely the finite difference version of the curl in Equation 1.4.3.

Finally, the total effective magnetic field at site $\{i,j\}$ is given by:

$$\mathbf{H}_{i,j}^{eff} = \mathbf{H}_{i,j}^{Exch} + \mathbf{H}_{i,j}^{Zee} + \mathbf{H}_{i,j}^{DMI} \quad (2.1.7)$$

2.2 System of Units

In order to provide physical meaning to simulation parameters, we developed a set of scaled quantities that would recast Equation 2.1.2 into a unit-less form.

First we define our energy scale to be the exchange coupling constant $J = 10^{-3}\text{eV}$. In this way, all other coupling constants in the Hamiltonian are written in units of J . Using the energy scale, we define our time scale \mathcal{T} to be:

$$\mathcal{T} = \frac{\mathcal{N}}{\gamma J} \quad (2.2.1)$$

For $\mathcal{N} = g\mu_B$ and $\gamma = g\mu_B/\hbar$:

$$\mathcal{T} = \frac{\hbar}{J} \sim 0.7\text{ps} \quad (2.2.2)$$

Finally, our length scale is determined by the lattice constant $a = 5\text{\AA}$. Using J, \mathcal{T} and a , one can non-dimensionalise Equation 2.1.2 to give:

$$\frac{\partial \mathbf{n}_{i,j}}{\partial \tau} = -\frac{1}{1+\alpha^2} [\mathbf{n}_{i,j} \times \mathbf{H}_{i,j}^{eff} + \alpha \mathbf{n}_{i,j} \times (\mathbf{n}_{i,j} \times \mathbf{H}_{i,j}^{eff})] \quad (2.2.3)$$

where $\tau = t/\mathcal{T}$. In using these scaled quantities, we have eliminated the microscopic constants γ and \mathcal{N} from the LLG equation, thus making the numerics less computationally intensive.

2.3 Developing the Simulation

The simulation used in this project was built in Python. Periodic boundary conditions are imposed using a modulo operation on the lattice indices:

$$\{(N+1)\text{mod}N, j\} \rightarrow \{1, j\}$$

The spin vectors of all lattice sites are stored in a single state-vector \mathbf{v} , as follows:

$$\mathbf{v} = [\mathbf{n}_{1,1}, \mathbf{n}_{1,2}, \dots, \mathbf{n}_{i,j}, \dots, \mathbf{n}_{N,N}]^T \quad (2.3.1)$$

A function `M_comp()` was written to take mesh-grids of n_x , n_y and n_z values and compile the $1 \times 3N^2$ vector \mathbf{v} . A second function `M_exp()` was also written to do the opposite of this process, decomposing \mathbf{v} into mesh-grids (see Electronic Appendix A).

In this way, one can express the cross products on the right-hand-side of Equation 2.2.3 as evolution matrices that act on \mathbf{v} . First, we note that for a general lattice vector $\mathbf{A}_{i,j}$:

$$\mathbf{A}_{i,j} \times \mathbf{n}_{i,j} = \hat{\mathbf{a}}_{i,j} \mathbf{n}_{i,j} = \begin{bmatrix} 0 & -A_{i,j}^z & A_{i,j}^y \\ A_{i,j}^z & 0 & -A_{i,j}^x \\ -A_{i,j}^y & A_{i,j}^x & 0 \end{bmatrix} \begin{bmatrix} n_{i,j}^x \\ n_{i,j}^y \\ n_{i,j}^z \end{bmatrix} \quad (2.3.2)$$

Therefore, computing the cross products for *all* lattice sites amounts to a matrix-vector multiplication:

$$\hat{\mathbf{A}}\mathbf{v} = \begin{bmatrix} \hat{\mathbf{a}}_{1,1} & & 0 \\ & \hat{\mathbf{a}}_{1,2} & \\ & & \ddots \\ 0 & & \hat{\mathbf{a}}_{N,N} \end{bmatrix} \begin{bmatrix} \mathbf{n}_{1,1} \\ \mathbf{n}_{1,2} \\ \vdots \\ \mathbf{n}_{N,N} \end{bmatrix} \quad (2.3.3)$$

where $\hat{\mathbf{A}}$ is a $3N^2 \times 3N^2$ matrix written in block form. The LLG equation, expressed in matrix-vector form, reads:

$$\frac{d\mathbf{v}}{d\tau} = \frac{1}{1+\alpha^2} [\hat{\mathbf{H}}_{eff} + \alpha \hat{\mathbf{N}}\hat{\mathbf{H}}_{eff}] \mathbf{v} \quad (2.3.4)$$

The micro-magnetic simulation involves solving the LLG equation in discrete time-steps $d\tau$ using SciPy's numerical ODE solver, up to a final time τ_f (see Electronic Appendix B). Matrices $\hat{\mathbf{N}}$ and $\hat{\mathbf{H}}_{eff}$ were generated at each time step using programmed functions `M_matrix()` and `H_matrix()` respectively (see Electronic Appendix A). With this formalism, the entire lattice of spins can be evolved over time without having to integrate each lattice site individually.

2.4 Single skyrmion initial condition

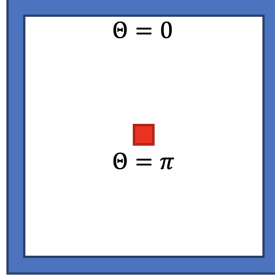


Figure 2.2: Boundary conditions for $\Theta(\rho)$ on a lattice. The central spin (red) is set to $\Theta = \pi$. The boundary spins (blue) are set to $\Theta = 0$.

In order to integrate Equation 2.1.2, one must supply an initial condition. We are primarily interested in single skyrmion initial conditions. One way to proceed is to supply an ansatz for the skyrmion profile that satisfies the boundary conditions (Equation 1.2.10). One such ansatz, developed by Wang *et al.* [26], is:

$$\Theta(r) = 2 \tan^{-1} \left\{ \frac{\sinh(R/w)}{\sinh(r/w)} \right\} \quad (2.4.1)$$

where R and w are variational parameters associated with the radius of the skyrmion ($\Theta(R) = \pi/2$) and width of skyrmion boundary respectively. An obvious pitfall with this method, is that one must pre-determine which values of R and w are favoured by the interaction strengths in Equation 2.1.1. Sub-optimal values for R and w will either result in destabilisation of the skyrmion, or unfavourable relaxation dynamics associated with the skyrmion relaxing to its equilibrium configuration.

In order to mitigate such effects, we numerically solve the Euler-Lagrange equation (Equation 1.2.9) by the relaxation method. This involves interpreting the Euler-Lagrange equation as an effective *time dependent* equation:

$$\frac{\partial \Theta}{\partial t} = \rho \frac{\partial^2 \Theta}{\partial \rho^2} + \partial_\rho \Theta - \frac{\sin 2\Theta}{2\rho} + 2 \sin^2 \Theta - \frac{ZJ}{D^2} \rho \sin \Theta \quad (2.4.2)$$

and solving for the steady state solution where $\dot{\Theta} = 0$. Since we are solving on a square lattice, we rewrite derivatives in Cartesian coordinates:

$$\partial_\rho \Theta = \cos \varphi \partial_x \Theta + \sin \varphi \partial_y \Theta \quad (2.4.3)$$

$$\partial_\rho^2 \Theta = \cos^2(\varphi) \partial_x^2 \Theta + \sin(2\Theta) \partial_x \partial_y \Theta + \sin^2(\varphi) \partial_y^2 \Theta \quad (2.4.4)$$

In this way, the radial derivatives can be discretized using finite difference formulas. These manipulations allow us to rewrite Equation 2.4.2 in the form:

$$\Theta_{i,j}(t + \delta t) = \Theta_{i,j}(t) + \delta t \frac{\partial \Theta_{i,j}}{\partial t} \quad (2.4.5)$$

where δt is an infinitesimal time step, and $\frac{\partial \Theta_{i,j}}{\partial t}$ is Equation 2.4.2 expressed in finite difference form. In order to match the boundary conditions illustrated in Figure 2.2,

the values of $\Theta_{i,j}$ are evolved using Equation 2.4.5 for all lattice points within the blue boundary. This process is repeated until a steady state condition is met. More formally, we require:

$$\max|\Theta(t + \delta t) - \Theta(t)| \leq 10^{-6} \quad (2.4.6)$$

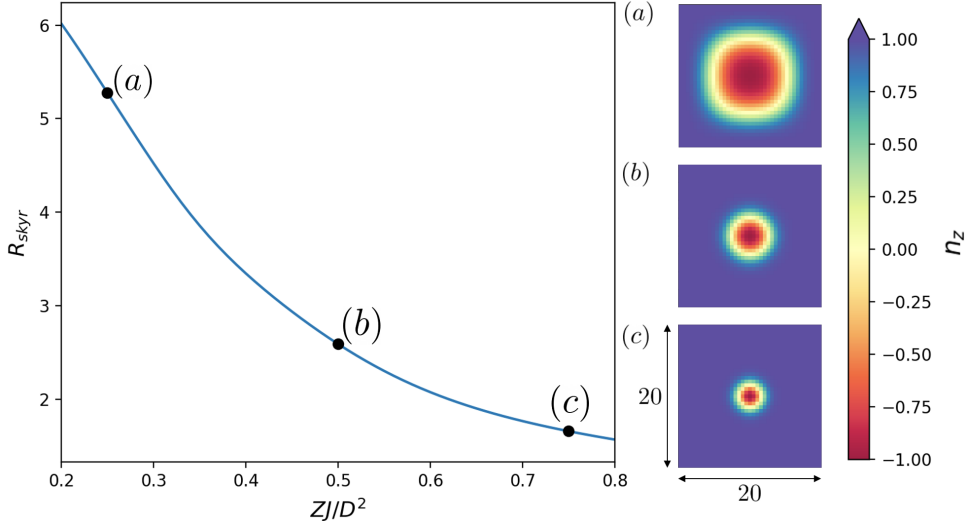


Figure 2.3: **Left:** Radius of skyrmion $R_{skyrmion}$ against ZJ/D^2 ($J = 1$, $D = 1$). **Right:** Numerically obtained skyrmion profiles for ZJ/D^2 values: (a) 0.25, (b) 0.5, and (c) 0.75. The colourbar gives spin z -components n_z .

Figures 2.3(a),(b) and (c) show the z -component of skyrmion profiles calculated using the relaxation method for a 39×39 lattice. The left panel of Figure 2.3 also gives the radius of the skyrmion $R_{skyrmion}$ for a range of coupling strengths ZJ/D^2 . We define $R_{skyrmion}$ by the solution to $\Theta(\rho) = \pi/2$. On a lattice, $R_{skyrmion}$ can be estimated by taking diametrical cuts across the lattice, before using a curve-fitting algorithm to approximate the radial profile of $\Theta_{i,j}$ by a continuous function $f(\rho)$. With this, one can obtain the radius by finding the root to $f(\rho) - \frac{\pi}{2} = 0$.

As expected, the radius of the skyrmion diminishes as ZJ/D^2 is increased. For higher Zeeman coupling, the ferromagnetic region is energetically favourable and grows in size, thus constricting the radius of the skyrmion. Furthermore, as described in Section 1.2.2, we observe the decay length to the ferromagnetic phase to be greater for smaller Z , resulting in a “softer” boundary profile.

2.5 Topological charge on a lattice

Often for diagnostic as well as investigative purposes, it is useful to calculate the total topological charge of the spin texture. In our investigations the topological charge was used to verify if the system was stabilising the correct skyrmionic textures. Instead of approximating Equation 1.3.1 using finite-difference formulas, we use the lattice generalisation

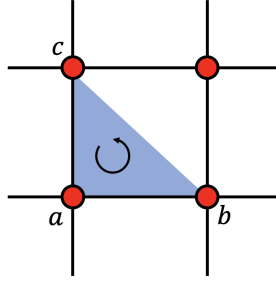


Figure 2.4: The topological charge is evaluated by summing over signed triangular plaquettes of the lattice. Image adapted from [27].

used by Kim *et al.* [27] and Berg *et al.* [28]:

$$\mathcal{Q} = -\frac{1}{2\pi} \sum_{(abc)} 2 \arctan \left\{ \frac{\mathbf{n}_a \cdot (\mathbf{n}_b \times \mathbf{n}_c)}{1 + \mathbf{n}_a \cdot \mathbf{n}_b + \mathbf{n}_a \cdot \mathbf{n}_c + \mathbf{n}_b \cdot \mathbf{n}_c} \right\} \quad (2.5.1)$$

where $\langle abc \rangle$ denotes a sum over signed triangular plaquettes of the lattice, as shown in Figure 2.4. Of course, a , b and c are each short-hand for lattice indices $\{i, j\}$, $\{i, j + 1\}$ and $\{i + 1, j\}$ respectively.

2.6 Decay Into Helical, SkX, or Ferromagnetic State

As validation for the micro-magnetic simulation, we showed our system decayed into one of three specific states mentioned in Section 1.2, depending on the strength of the external magnetic field. These three states are routinely described in the literature, thus providing a simple test for simulation validity [29][30].

In what follows, we simulate on a lattice of 21×21 spins. The initial conditions for each spin component were chosen as:

$$\begin{aligned} n_x &= \sin x \cos y \\ n_y &= \sin x \sin y \\ n_z &= \cos x \end{aligned}$$

where $x = y = [-10; 10]$. These initial conditions are topologically trivial ($\mathcal{Q} = 0$) and induce sufficient curvature in the spin-texture to observe either the helical, skyrmion or ferromagnetic phase. In order to allow the system to reach a steady state, we simulated for a total time $\tau_f = 600$ with time steps $d\tau = 0.05$.

The magnetic field strength is controlled by the parameter Z in the micromagnetic Hamiltonian. In producing the phase plot shown in Figure 2.5, the ferromagnetic state is detected when the system meets the following condition:

$$\left| 1 - \frac{\mathbf{v}(\tau_f) \cdot \mathbf{v}_{FM}}{\|\mathbf{v}(\tau_f)\| \|\mathbf{v}_{FM}\|} \right| \leq 10^{-1} \quad (2.6.1)$$

where $\mathbf{v}(\tau_f)$ is the state-vector at time τ_f , and \mathbf{v}_{FM} is a ferromagnetic state-vector. The presence of topological textures in the system is easily detected when $\mathcal{Q} \in \mathbb{Z}$.

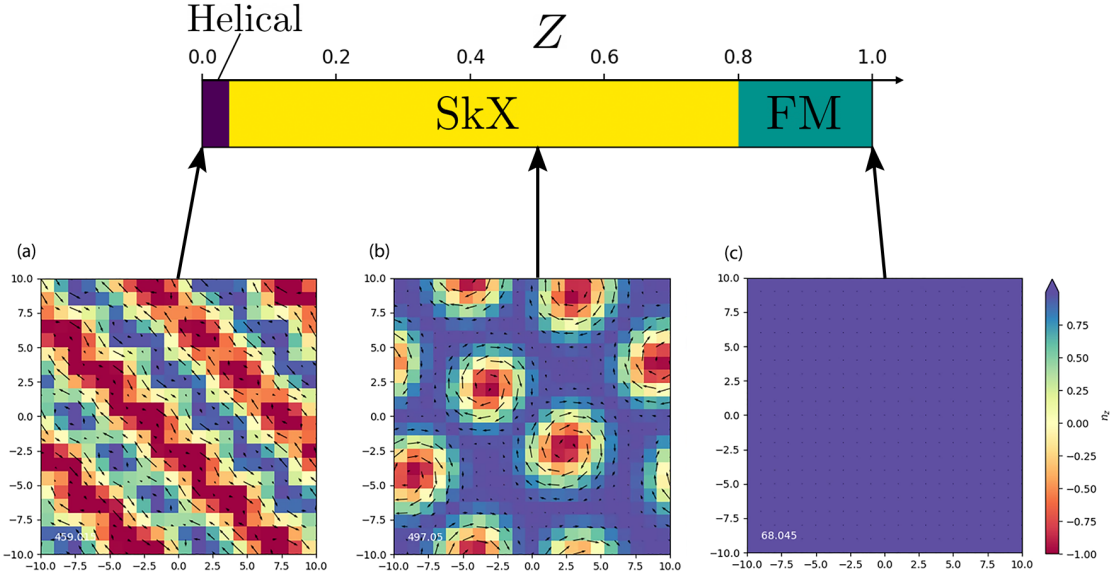


Figure 2.5: **Top:** Phase plot of the system for a range of Zeeman coupling Z . Final states of the system: (a) Helical state (HL) for $Z = 0$, (b) Skyrmiion lattice phase (SkX) for $Z = 0.5$ (c) Ferromagnetic state (FM) for $Z = 1$. $J = D = 1$ and $\alpha = 0.04$ for all three scenarios.

At zero and low external magnetic fields, the competition between exchange and DM interaction causes the system to stabilise the helical state as shown in Figure 2.5(a). Moreover, we find the spin-spiral wavelength to be $\lambda \approx 6\sqrt{2}$. This differs from the continuum prediction of Equation 1.2.5 by roughly a factor of $\sqrt{2}$. Deviations from the continuum theory are expected, since we are simulating on a very coarse lattice.

The phase diagram shows that even a slight increase in Zeeman coupling can destabilise the helical domains. As shown in Figure 2.5(b), for $Z = 0.5$, the helical domains proliferate to form multiple skyrmions. The total topological charge in Figure 2.5(b) is 6. This qualitatively resembles the skyrmion lattice (SkX) phase reported in the literature [31][7], where skyrmions pack into a hexagonal crystal arrangement. In our simulation, the hexagonal arrangement is not so perfect. This asymmetry can be attributed to the small size of the system and periodic boundary conditions, which allow skyrmions at opposite edges of the system to “repel”, thus preventing long range periodic order from occurring. Physically, skyrmion-skyrmion repulsion should stem from the domain wall energy increasing as two skyrmions are pushed together. Therefore, we expect the repulsive effect to be strongest when the separation between the skyrmion boundaries d is comparable to the decay length l [32]. That is:

$$d \approx \sqrt{\frac{J}{Z}} \quad (2.6.2)$$

For $Z = 0.5$, the effect of skyrmion repulsion is strongest when $d \approx \sqrt{2}$, which agrees with the closest observed separation between skyrmions in Figure 2.5(b).

As the Zeeman coupling strength is further increased, the skyrmion radii decrease, in agreement with the results of Section 2.4. Their boundaries became harder as more spins aligned with the external magnetic field due to the increasing Zeeman interaction. At

$Z = 1$, the Zeeman interaction completely dominates over the exchange and DM interactions, causing the spins at each lattice site to align with the external magnetic field. This produces the ferromagnetic state shown in Figure 2.5(c).

Chapter 3

Pulsed Dynamics

In what follows, we use our micro-magnetic simulation to study the pulsed dynamics of single skyrmions.

3.1 Out-of-Plane Pulses

A study orchestrated by Mochizuki *et al.* identifies three vibrational modes of a skyrmion excited via the application of a magnetic pulse. The collective excitation of these modes leads to the melting of a skyrmion crystal [29]. Motivated by that investigation, we aimed to observe the three aforementioned internal modes and explore the role they play in skyrmion deformation.

Prior to applying the out-of-plane magnetic pulse, a single-skyrmion initial condition was calculated using the method described in Section 2.4. Since this method relies on solving an equation derived from the continuum theory, we observed small amplitude relaxation dynamics associated with finite-difference error. Therefore, the skyrmion was allowed to relax to its energetically favourable configuration, in order to prevent the relaxation dynamics superposing with the internal mode excitations. During this relaxation period, we monitor the difference in the z -component of the magnetisation between successive time-steps. For the magnetic pulse to be triggered, we require:

$$\langle |M_z(t + \delta t) - M_z(t)| \rangle_{600} \leq 10^{-7} \quad (3.1.1)$$

Where $\langle \dots \rangle_{600}$ denotes averaging over the last 600 time-steps and M_z is the z -component of the magnetisation, defined by:

$$\mathbf{M} = \frac{1}{N^2} \sum_{i=1}^N \sum_{j=1}^N \mathbf{n}_{i,j} \quad (3.1.2)$$

Once the relaxation condition is satisfied, an out-of-plane magnetic field pulse directed along $\hat{\mathbf{e}}_z$ is applied to the system for one time-step. The out-of-plane pulse excited a breathing mode of the skyrmion, resulting in damped harmonic motion of the skyrmion radius, as shown by snapshots in Figure 3.1. The associated time evolution of the out-of-plane magnetisation is shown in Figure 3.2. The initial oscillations in the out-of-plane magnetisation correspond to the relaxation dynamics of the skyrmion. Visually we find that this constitutes small amplitude radial oscillations and low frequency modulations of the domain wall width.

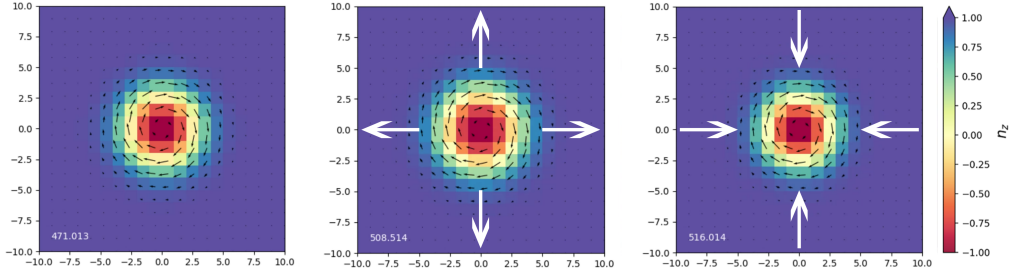


Figure 3.1: Chronological snapshots of radial breathing mode excited by in-plane magnetic pulse. Unitless time τ is given at bottom-left of each snapshot. Micro-magnetic parameters: $J = 1$, $D = 1$, $Z = 0.5$ and $\alpha = 0.04$.

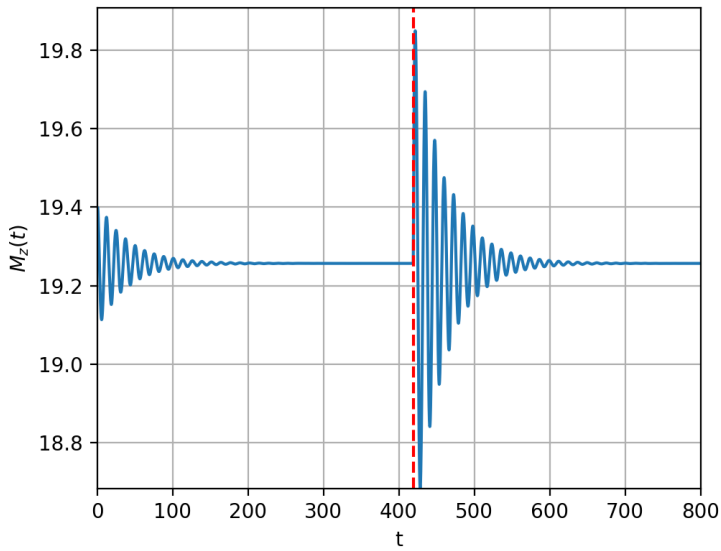


Figure 3.2: Plot of the out-of-plane magnetisation $M_z(t)$ as a function of time. The red dashed line indicates when the out-of-plane magnetic pulse was applied to the system.

Eventually the amplitude of these oscillations approaches zero, indicating that the skyrmion has reached steady state. The red dashed line indicates the application of the out-of-plane magnetic pulse. Once applied, we observe exponentially damped oscillations in M_z .

We plot the absorption spectrum of the spin system by calculating $\text{Im}[\mathbf{M}(\omega)]$. In doing so, we only Fourier transform the post-pulse portion of the signal. Naturally, for the out-of-plane pulse, only $M_z(\omega)$ exhibits an absorption peak. Figure 3.3(Left) shows the absorption spectra for 4 different Zeeman coupling values. At each Z -value, a prominent resonance peak is observed corresponding to the excited breathing mode. Upon reinstating units using time scale \mathcal{T} (Equation 2.2.2), we find that frequencies are of order 100GHz, thus placing them in the microwave regime.

The height of the resonance diminishes with increasing Z . Physically, this tells us that the skyrmion becomes stiffer at larger magnetic fields due to the larger energy penalty associated with changes in the radius. Additional smaller resonances are found either side of the main resonance, which we attribute to residual relaxation oscillations superposing

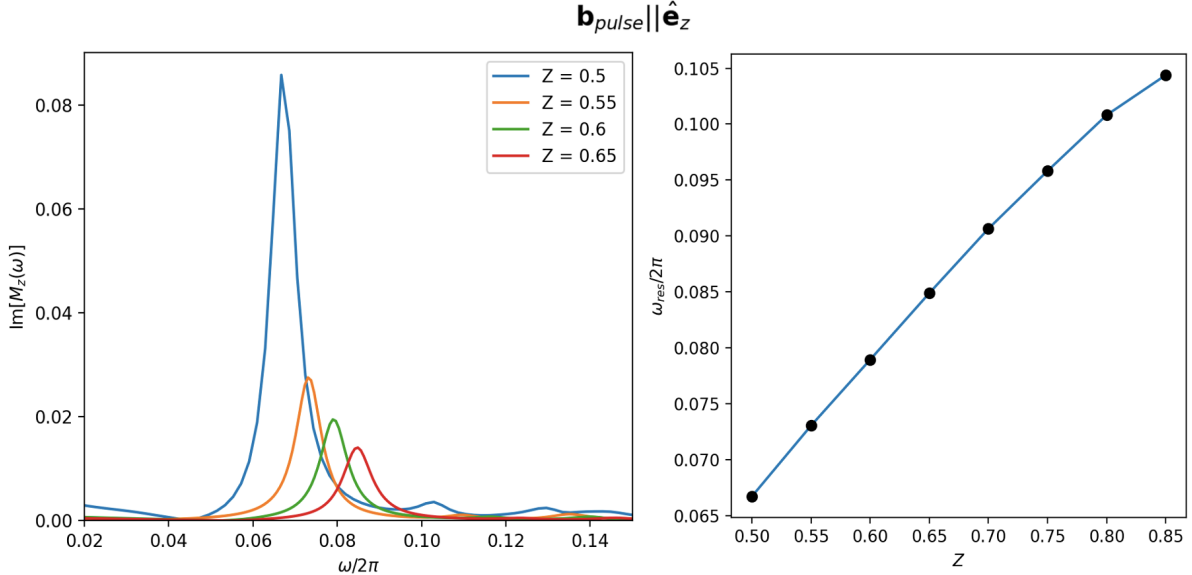


Figure 3.3: **Left:** The frequency spectrum of the system plotted for 4 values of the Zeeman coupling strength Z . **Right:** Resonant frequency of radial oscillations ω_{res} against Z . $J = 1, D = 1, \alpha = 0.04$

with the dominant signal. As shown in Figure 3.3(Right) we observe the resonant frequency ω_{res} increasing as the Zeeman coupling strength is increased. This opposes the trend described in the Mochizuki investigation, where the resonant frequency decreased upon increasing the Zeeman coupling strength [29].

In what follows, we corroborate our observations using scaling relations based on the continuum Hamiltonian (Equation 1.2.1). The Hamiltonian contribution from the DM interaction is:

$$\mathcal{H}_{DMI} = D \int dx dy \mathbf{n} \cdot (\nabla \times \mathbf{n}) \sim DR \quad (3.1.3)$$

which scales linearly with the skyrmion radius R . The Zeeman contribution to the Hamiltonian is given by:

$$\mathcal{H}_{Zee} = Z \hat{\mathbf{b}} \int d^2x n_z \sim Z R^2 \quad (3.1.4)$$

and so scales quadratically with the skyrmion radius, where n_z is the z-component of the magnetic dipole moment and $\hat{\mathbf{b}}$ is the unit vector specifying the direction of the external magnetic field. Using these scaling relations, the skyrmion energy as a function of the skyrmion radius can be expressed as:

$$E_{sky}(R) \sim E_0 - aDR + bZR^2 \quad (3.1.5)$$

where E_0 , a and b are numerical constants that arise from the explicit evaluation of the exchange, DM and Zeeman integrals in Equation 1.2.1. The DM term requires a negative sign since the DM interaction favours skyrmionic textures.

The total skyrmion energy function in equation 3.1.5 is plotted against the skyrmion radius in figure 3.4. $E_{sky}(R)$ has a minimum at the equilibrium radius:

$$R_0 \sim \frac{aD}{2bZ} \quad (3.1.6)$$

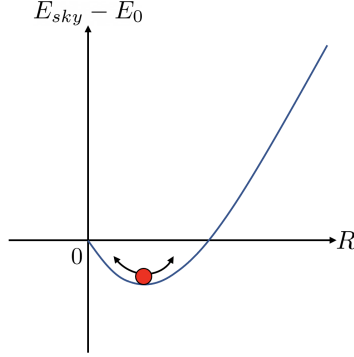


Figure 3.4: Perturbations around the minimum of $E_{sky}(R)$ correspond to the radial breathing modes observed.

where around the minimum, the function is parabolic. A perturbation around this minimum caused by an out-of-plane magnetic pulse will set the radius of the skyrmion into simple harmonic motion (SHM) around the equilibrium radius. This corresponds to the breathing mode, where the oscillations of the skyrmion radius are damped due to the non-zero Gilbert damping constant α .

An effective spring constant for the system can be found by calculating a Taylor expansion of $E_{sky}(R)$ around the equilibrium radius R_0 :

$$E_{sky}(R) \sim E_{sky}(R_0) + \frac{1}{2}E''_{sky}(R_0)R^2 \quad (3.1.7)$$

Comparing this with the total energy of a harmonic oscillator, the effective spring constant for the skyrmion is found to be equal to $E''_{sky}(R_0)$.

This gives an effective spring constant:

$$k \sim 2bZ \quad (3.1.8)$$

which scales linearly with the Zeeman coupling strength. This relation also agrees with Figure 3.3(Right), which demonstrates a roughly linear relationship between the resonant frequency and the Zeeman coupling. We also expect this on physical grounds, since for higher Zeeman coupling, there is a larger energy penalty associated with small fluctuations of the skyrmion radius, resulting in a higher restoring force. Therefore, an increased Zeeman coupling strength leads to an increased effective spring constant, which would correspond to an increased oscillation frequency.

3.2 In-Plane Pulses

We now investigate the use of an in-plane magnetic pulse. As before, this pulse was applied for a single time-step once the skyrmion had sufficiently relaxed, but was now directed along \hat{e}_x . The absorption spectra for different Z values are shown in Figure 3.6(Left). Each contains a single resonance corresponding to counter-clockwise rotation of the skyrmion core, as shown in Figure 3.5.

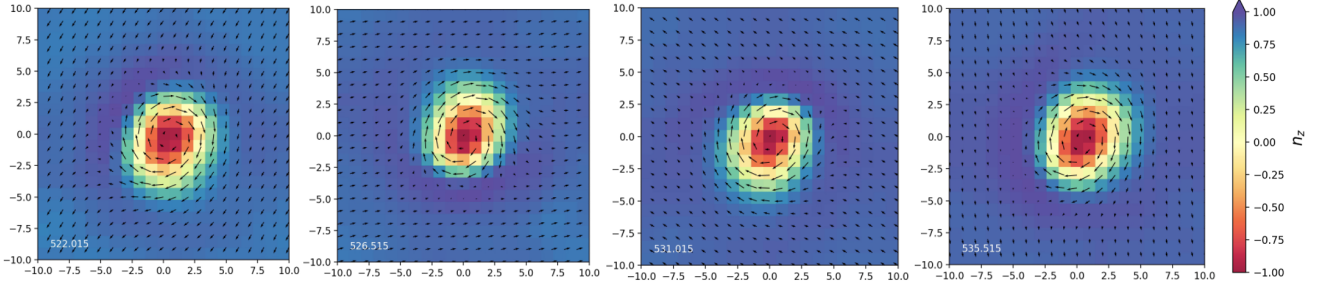


Figure 3.5: Chronological snapshots of counter-clockwise rotational mode excited by in-plane magnetic pulse. Unitless time τ is given at bottom-left of each snapshot. Micro-magnetic parameters: $J = 1$, $D = 1$, $Z = 0.5$ and $\alpha = 0.04$.

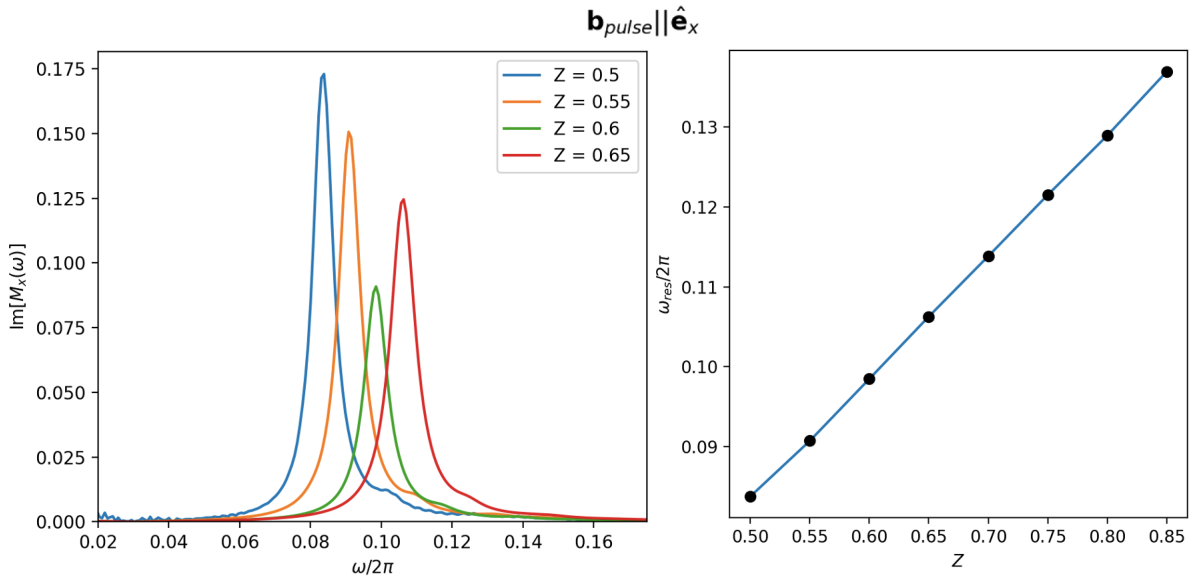


Figure 3.6: **Left:** The frequency spectrum of the system with the applied in-plane magnetic pulse, plotted for 4 values of the Zeeman coupling strength Z . **Right:** Resonant frequency of rotational oscillations ω_{res} against Z . $J = 1, D = 1, \alpha = 0.04$.

From the spectra, we note that the resonant frequency of the rotational modes are higher than those of the radial breathing modes for the same value of Z . This allows us to conclude that asymmetric distortions of the skyrmion come with a higher energy penalty than those which respect the azimuthal symmetry of the skyrmion profile.

From the Mochizuki investigation, our expectation was to also observe a second, clockwise rotational mode when excited by the in-plane pulse [29]. Several similar studies have also observed at least two modes in the excitation spectra for in-plane pulses [33][12][10][11]. For this reason, the absorption spectrum was expected to consist of two resonance peaks, with the lower-frequency resonance corresponding to a counter-clockwise rotational mode of the skyrmion. The higher-frequency resonance would correspond to a higher-energy clockwise rotational mode. The absence of the clockwise mode is a clear difference between our observations and those in the literature.

3.3 Missing resonances and Skyrmion Mass

In what follows, we propose an explanation for the absence of the clockwise mode in our simulations. As a starting point, we consider a toy model, which qualitatively shares many similarities with the skyrmion rotational modes observed in the literature. Stated as a differential equation, this model reads:

$$M \begin{bmatrix} \ddot{\mathcal{X}} \\ \ddot{\mathcal{Y}} \end{bmatrix} + \begin{bmatrix} 0 & -G \\ G & 0 \end{bmatrix} \begin{bmatrix} \dot{\mathcal{X}} \\ \dot{\mathcal{Y}} \end{bmatrix} + \begin{bmatrix} \Gamma & 0 \\ 0 & \Gamma \end{bmatrix} \begin{bmatrix} \dot{\mathcal{X}} \\ \dot{\mathcal{Y}} \end{bmatrix} + K \begin{bmatrix} \mathcal{X} \\ \mathcal{Y} \end{bmatrix} = \mathbf{f}(t) \quad (3.3.1)$$

where $\{\mathcal{X}, \mathcal{Y}\}$ are collective coordinates that track the centre of the skyrmion. M is the skyrmion “mass”. G is a gyrocoupling constant which causes rotation of the skyrmion centre and K is an effective spring constant. Γ is a damping coefficient, which causes the centre of the skyrmion to spiral into the origin and $\mathbf{f}(t)$ is a driving force.

In the context of this toy-model, an in-plane pulse in the \hat{e}_x direction is emulated by an impulse driving force:

$$\mathbf{f}(t, t') = \begin{bmatrix} \delta(t - t') \\ 0 \end{bmatrix} \quad (3.3.2)$$

Therefore, solving Equation 3.3.1 amounts to calculating the Green’s functions of this theory. To make contact with the absorption spectrum, we choose to calculate the spectral Green’s functions, $\mathcal{X}(\omega, t')$ and $\mathcal{Y}(\omega, t')$. Taking the Fourier transform of both sides yields the following matrix equation:

$$\begin{bmatrix} -M\omega^2 + i\omega\Gamma + K & -i\omega G \\ i\omega G & -M\omega^2 + i\omega\Gamma + K \end{bmatrix} \begin{bmatrix} \mathcal{X}(\omega, t') \\ \mathcal{Y}(\omega, t') \end{bmatrix} = \begin{bmatrix} e^{i\omega t'} \\ 0 \end{bmatrix} \quad (3.3.3)$$

Inverting the above dynamical matrix, we obtain the Green’s functions:

$$|\mathcal{X}(\omega, t')|^2 = \frac{(-M\omega^2 + K)^2 + \omega^2\Gamma^2}{\{(-M\omega^2 + K)^2 - \omega^2(G^2 + \Gamma^2)\}^2 + 4\omega^2\Gamma^2(-M\omega^2 + K)^2} \quad (3.3.4)$$

$$|\mathcal{Y}(\omega, t')|^2 = \frac{\omega^2 G^2}{\{(-M\omega^2 + K)^2 - \omega^2(G^2 + \Gamma^2)\}^2 + 4\omega^2\Gamma^2(-M\omega^2 + K)^2} \quad (3.3.5)$$

We are primarily interested in $|\mathcal{X}(\omega, t')|^2$ since it is analogous to the numerically calculated magnetisation absorption spectra $\text{Im}[M_x(\omega)]$. As shown in Figure 3.7, $|\mathcal{X}(\omega, t')|^2$ exhibits two resonances at frequencies:

$$\omega_{\pm} = -\frac{G}{2M} \pm \sqrt{\left(\frac{G}{2M}\right)^2 + \frac{K}{M}} \quad (3.3.6)$$

The lower energy resonance corresponds to a counter-clockwise rotational mode with frequency ω_+ , whilst the higher energy resonance at ω_- corresponds to the clockwise mode. The splitting between these peaks is given by:

$$\Delta\omega = |\omega_-| - |\omega_+| = \frac{G}{M} \quad (3.3.7)$$

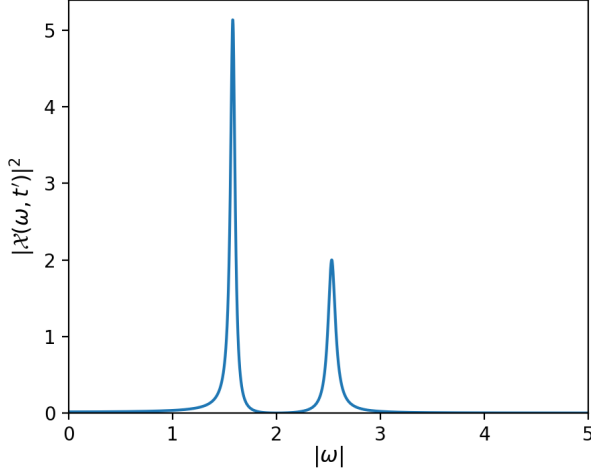


Figure 3.7: Spectral Green's function $|\mathcal{X}(\omega, t')|^2$ for $M = 2$, $G = 1.9$, $\Gamma = 0.14$, $K = 8$.

Interestingly as $M \rightarrow 0$, we find $\Delta\omega \rightarrow \infty$, leaving only a *single* resonance in the spectrum. In the massless limit, the equation of motion reduces to:

$$\begin{bmatrix} \dot{\mathcal{X}} \\ \dot{\mathcal{Y}} \end{bmatrix} = \frac{K}{\Gamma^2 + G^2} \begin{bmatrix} -\Gamma & -G \\ G & -\Gamma \end{bmatrix} \begin{bmatrix} \mathcal{X} \\ \mathcal{Y} \end{bmatrix} \quad (3.3.8)$$

The off-diagonal elements of the matrix reveal that this resonance corresponds to counter-clockwise motion only. Therefore, in the massless limit, the clockwise mode is absent.

Surprisingly, this simple model emerges naturally when one tackles the underlying micromagnetics of the rotational mode problem. Makhfudz *et al.* have shown that Equation 3.3.1 can be derived using the method of collective coordinates described in Section 1.5[34]. In doing so, the authors were able to make contact between the toy-model parameters (M, G) and the underlying micromagnetic parameters (γ, \mathcal{N} etc.). We shall now briefly review their approach, before extending the salient result to suggest why the skyrmions simulated in this thesis may have negligible mass.

For studying the rotational mode problem, it is useful to describe the modes in terms of a locus $r(\varphi, t)$ where spins lie in-plane. For an un-perturbed skyrmion $r(\varphi, t) = R$, where R is the skyrmion radius. Perturbations to this locus can be readily expressed as a Fourier series:

$$r(\varphi, t) = R + \sum_{n=-\infty}^{\infty} r_n(t) e^{in\varphi} \quad (3.3.9)$$

where $r_n = r_{-n}^*$. In this way, $n = 0$ characterises the radial breathing modes of Section 3.1, whilst $n = \pm 1$ characterises small displacements of the skyrmion core if we take:

$$r_{\pm 1}(t) = \frac{\mathcal{X}(t) \mp i\mathcal{Y}(t)}{2} \quad (3.3.10)$$

One can also consider fluctuations to the *angle* of the in-plane spins ψ in a similar manner (see Figure 3.8):

$$\psi(\varphi, t) = \varphi - \frac{\pi}{2} + \sum_{n=-\infty}^{\infty} \psi_n(t) e^{in\varphi} \quad (3.3.11)$$

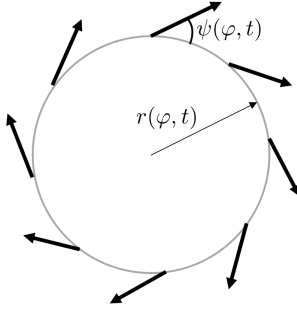


Figure 3.8: Schematic diagram of locus of in-plane spins $r(\varphi, t)$ and in-plane spin angle $\psi(\varphi, t)$.

where we have chosen the angle of the ground state spins to be $\varphi - \pi/2$, since this describes the Bloch skyrmions investigated throughout this chapter. In this description, it is natural to treat the Fourier coefficients as time-dependent collective coordinates $\xi(t) = \{r_n, \psi_n\}$. Makhfudz *et al.* rightly point out that the r and ψ Fourier coefficients are coupled to each-other, since excitations in the radius of the skyrmion may cause fluctuations of the in-plane angle. This consideration warrants the following expression for the collective coordinate Lagrangian given in Equation 1.5.6:

$$\mathcal{L}[r, \psi] = R \int_0^{2\pi} d\varphi g \dot{r} \psi - \mathcal{H}[r, \psi] \quad (3.3.12)$$

where $g = 2\mathcal{N}/\gamma$. Upon plugging the mode expansions of Equations 3.3.9 and 3.3.11 into this Lagrangian, one can obtain a Lagrangian for the Fourier coefficients only:

$$\mathcal{L}[r_n] = \sum_n \left(\frac{\pi g^2 R}{\kappa} |\dot{r}_n|^2 + 2\pi i n g r_n^* \dot{r}_n \right) - \mathcal{H}[r] \quad (3.3.13)$$

where κ is the spring constant for fluctuations of the in-plane angle away from the tangential direction. Interestingly, if one only considers the $n = \pm 1$ terms, the Lagrangian reads:

$$\mathcal{L} = \frac{\pi g^2 R}{2\kappa} (\dot{\mathcal{X}}^2 + \dot{\mathcal{Y}}^2) + \frac{2\pi g}{2} (\mathcal{X} \dot{\mathcal{Y}} - \mathcal{Y} \dot{\mathcal{X}}) - \frac{K}{2} (\mathcal{X}^2 + \mathcal{Y}^2) \quad (3.3.14)$$

where we have assumed a quadratic restoring potential for $\mathcal{H}[\mathcal{X}, \mathcal{Y}]$, with spring stiffness K . Variation of Equation 3.3.14 yields the same toy-model described by Equation 3.3.1, if one takes:

$$M = \frac{\pi g^2 R}{\kappa} \quad (3.3.15)$$

$$G = 2\pi g \quad (3.3.16)$$

The Lagrangian in Equation 3.3.14 has neglected dissipative effects since it does not affect the rotational dynamics. In principle, it can be added through a Rayleigh dissipative functional [25]. A detailed derivation of Equations 3.3.12 and 3.3.13 is given in their original paper [34]. Equation 3.3.15 implies that the skyrmion mass depends on the stiffness of the in-plane spin angle κ .

Since κ is associated with the energy penalty due to fluctuations of ψ , we can gain intuition for its dependence on the Hamiltonian parameters by expanding \mathcal{H} around the

equilibrium angle $-\pi/2$. To do this, we substitute the skyrmion zenith angle profile $\Theta(\rho)$ and azimuthal angle $\Phi(\varphi) = \phi - \pi/2 - \psi$ into the continuum Hamiltonian of Equation 1.2.1. We find that only the DM contribution to the Hamiltonian density depends on the perturbation ψ :

$$D\mathbf{n} \cdot (\nabla \times \mathbf{n}) = -D \sin\left(\psi + \frac{\pi}{2}\right) \left[\frac{d\Theta}{d\rho} + \frac{\sin(2\Theta)}{2\rho} \right] \quad (3.3.17)$$

Expanding the trigonometric factor for small ψ , we obtain:

$$D\mathbf{n} \cdot (\nabla \times \mathbf{n}) = -D \left[\frac{d\Theta}{d\rho} + \frac{\sin(2\Theta)}{2\rho} \right] \left(1 - \frac{1}{2}\psi^2 + \dots \right) \quad (3.3.18)$$

This tells us that small fluctuations of the in-plane spin angle will be energetically penalised by the DM interaction, but not the exchange or Zeeman interactions. Therefore, we speculate that the DM interaction is the dominant contributor to the κ factor. We would also expect this on physical grounds, since the DM interaction favours a specific chirality of the spin-texture. Since our simulations have used a large value for the DM constant ($D = J = 1$), we suspect this played a role in decreasing M , thus suppressing the clockwise mode peak in the absorption spectra. In contrast, previous investigations of pulsed skyrmion dynamics have used $D/J \ll 1$, which would not only yield much larger skyrmions, but also reduce the energy penalty associated with fluctuations of the in-plane spin angle [33][12][10][11].

3.4 Summary

In this chapter, we have investigated the breathing and rotational modes of a skyrmion. Using an out-of-plane magnetic pulse, a breathing mode of the skyrmion was excited where the skyrmion radius was seen to oscillate harmonically. It was observed that the associated resonant frequency increased with increasing Zeeman coupling. This observation was supported using a scaling relations argument. For an applied in-plane magnetic pulse, a counter-clockwise rotational mode of the skyrmion was excited but its higher-energy clockwise counter-part remained unobserved. Using a toy model, the possibility of a negligible skyrmion mass was determined. We propose that the large DM interaction strength used throughout this project was causing a large energy penalty for in-plane spin angle fluctuations, in turn decreasing the skyrmion mass M . This we believe, was suppressing the clockwise mode resonance peak.

Chapter 4

Instabilities and Magnon modes

In addition to exhibiting breathing and rotational modes, magnetic skyrmions can also spontaneously deform for certain values of magnetic field. In this chapter, we investigate two such deformations, which cause the skyrmion to deviate from its circular geometry.

4.1 Geometric Instabilities

For Zeeman coupling in range $0.5 \leq Z < 0.6$, the skyrmion was found to exhibit an elliptical instability upon excitation by an in-plane magnetic field pulse. The damped rotational mode is almost immediately followed by an elliptical instability where the skyrmion spontaneously elongates. Figure 4.1 shows four representative snapshots of this instability for $Z = 0.5$, which eventually causes the skyrmion to extend across the entire system. The skyrmion can be seen to wrap around the system due to periodic boundary conditions.

For $Z \leq 0.3$ we observe a spontaneous quadrupolar deformation of the skyrmion, propagating along the boundary in the counter-clockwise direction. As shown in Figure 4.2, the amplitude of this wave magnifies in time, until the skyrmion fragments into smaller, elongated skyrmions.

For both instabilities, the resulting spin textures are so-called *bi-merons*, which have been predicted to condense for low magnetic fields [35][36][17]. Physically these textures consist of two half-skyrmions ($\mathcal{Q} = 1/2$) connected by a topologically trivial, rectangular stripe domain ($\mathcal{Q} = 0$). The final state in Figure 4.2 consists of two bi-merons.

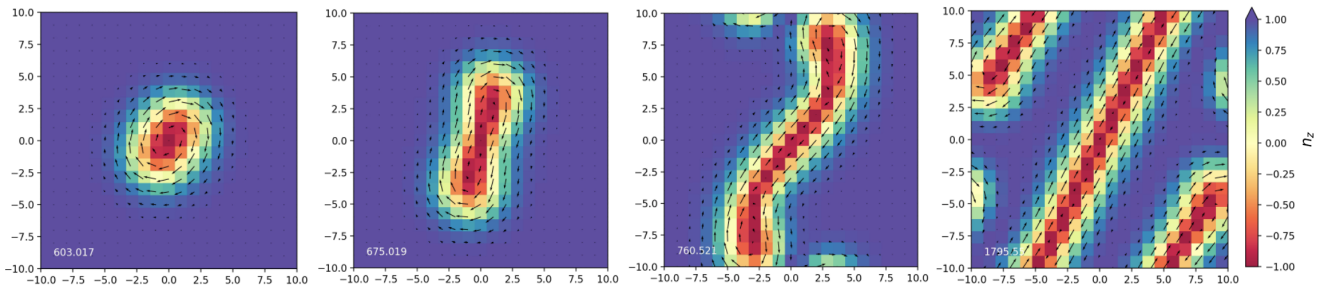


Figure 4.1: Elliptical instability of skyrmion, upon excitation by an in-plane magnetic field pulse. $J = 1$, $D = 1$ and $Z = 0.5$

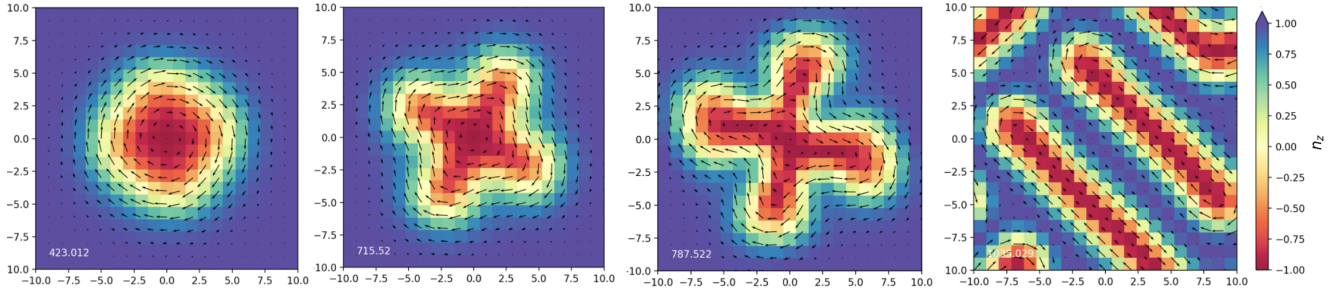


Figure 4.2: Spontaneous quadrupolar instability of skyrmion $J = 1$, $D = 1$ and $Z = 0.3$

Such geometric deformations have been investigated in the context of bound *magnon* modes of the skyrmion. Notably, the works of Lin *et al.*[6] and Schütte *et al.*[21] have numerically and analytically shown that the low energy fluctuation modes of the skyrmion resemble polygonal deformations. Furthermore, at critical magnetic fields, they found that the eigen-energy of the elliptical mode goes to zero. This observation has led authors to suggest that gapless magnon modes could explain certain polygonal instabilities of the skyrmion for low magnetic field strengths [37]. In the following sections, we investigate whether explanations based on gapless magnon modes could explain our instabilities shown in Figures 4.1 and 4.2, by numerically calculating the magnon spectrum.

4.2 The magnon problem

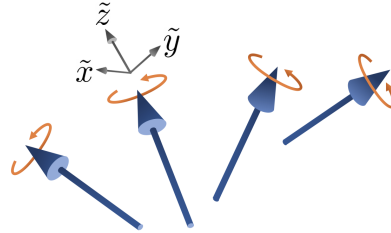


Figure 4.3: Local coordinate approach for magnon problem in non-colinear spin textures.

Physically, magnons correspond to fluctuations of the ground state spin texture. When canonically quantised, these fluctuation modes can be thought of as quasiparticles, hence the name “magnon”. We would like to stress that our usage of this term refers only to the classical case, since our spins are classical vectors. We now outline how one can calculate magnon modes for the skyrmion ground state.

In formulating the magnon problem, we follow the treatment given in: [6] and [38]. For such non-colinear ground states, it is simpler to rotate into a local coordinate frame \tilde{F} where the \tilde{z} -axis is aligned with the spin direction \mathbf{n} , as shown in Figure 4.3. This is achieved by an $SO(3)$ rotation matrix \mathcal{R} :

$$\mathcal{R} = \begin{bmatrix} -\sin \Phi & -\cos \Theta \cos \Phi & \sin \Theta \cos \Phi \\ \cos \Phi & -\cos \Theta \sin \Phi & \sin \Theta \sin \Phi \\ 0 & \sin \Theta & \cos \Theta \end{bmatrix} \quad (4.2.1)$$

where Θ and Φ are position dependent. This matrix relates the un-rotated spins \mathbf{n} to the rotated frame spins $\tilde{\mathbf{n}}$ by:

$$\mathbf{n} = \mathcal{R}\tilde{\mathbf{n}}$$

One can easily check that for $\tilde{\mathbf{n}} = [0, 0, 1]^T$, $\mathcal{R}\tilde{\mathbf{n}}$ is the skyrmion ground state given in Equation 1.2.6. Therefore, in the rotated frame $\tilde{n}_z = 1$ everywhere. In this scheme, small fluctuations are characterised by:

$$\begin{aligned}\tilde{n}_x &= \int d\omega \tilde{n}_x(\omega) e^{i\omega t} \\ \tilde{n}_y &= \int d\omega \tilde{n}_y(\omega) e^{i\omega t} \\ \tilde{n}_z &= 1 + \mathcal{O}(\tilde{\mathbf{n}}^2)\end{aligned}$$

In this way, the spin vectors can be decomposed into the ground-state vector \mathbf{n}_0 , along with a perturbation $\delta\mathbf{n}$:

$$\mathbf{n} = \underbrace{\begin{bmatrix} \tilde{n}_z \sin \Theta \cos \Phi \\ \tilde{n}_z \sin \Theta \sin \Phi \\ \tilde{n}_z \cos \Theta \end{bmatrix}}_{\mathbf{n}_0} + \underbrace{\begin{bmatrix} -\tilde{n}_x \sin \Phi - \tilde{n}_y \cos \Theta \cos \Phi \\ \tilde{n}_x \cos \Phi - \tilde{n}_y \cos \Theta \sin \Phi \\ \tilde{n}_y \sin \Theta \end{bmatrix}}_{\delta\mathbf{n}} \quad (4.2.2)$$

Our goal is to expand the Hamiltonian \mathcal{H} , given by Equation 2.1.1, in orders of the perturbation and plug the resulting expression into the LLG equation. The zeroth order contribution $\mathcal{H}^{(0)}$ is trivial, since it is simply the total energy of the skyrmion texture. Therefore, $\mathcal{H}^{(0)}$ has no dependence on \tilde{n}_x or \tilde{n}_y . It only depends on \tilde{n}_z values at each lattice site. The second-order contribution $\mathcal{H}^{(2)}$ is given by [6]:

$$\begin{aligned}\mathcal{H}^{(2)} = & -J \sum_{\mathbf{r}} \sum_{\mathbf{r}'} \tilde{n}_{\mathbf{r}}^y \{ \tilde{n}_{\mathbf{r}'}^y \mathcal{C}_{\mathbf{r}} \mathcal{C}_{\mathbf{r}'} \cos(\Phi_{\mathbf{r}} - \Phi_{\mathbf{r}'}) + \tilde{n}_{\mathbf{r}'}^y \mathcal{S}_{\mathbf{r}} \mathcal{S}_{\mathbf{r}'} - \tilde{n}_{\mathbf{r}'}^x \mathcal{C}_{\mathbf{r}} \sin(\Phi_{\mathbf{r}} - \Phi_{\mathbf{r}'}) \} \\ & + \tilde{n}_{\mathbf{r}}^x \{ \tilde{n}_{\mathbf{r}}^x \cos(\Phi_{\mathbf{r}} - \Phi_{\mathbf{r}'}) + \tilde{n}_{\mathbf{r}'}^y \mathcal{C}_{\mathbf{r}'} \sin(\Phi_{\mathbf{r}} - \Phi_{\mathbf{r}'}) \} \\ & + D \sum_{\mathbf{r}} \tilde{n}_{\mathbf{r}}^y \tilde{n}_{\mathbf{r}+ae_x}^y \{ \mathcal{C}_{\mathbf{r}+ae_x} \mathcal{S}_{\mathbf{r}} \sin \Phi_{\mathbf{r}+ae_x} - \mathcal{C}_{\mathbf{r}} \mathcal{S}_{\mathbf{r}+ae_x} \sin \Phi_{\mathbf{r}} \} + \{ \tilde{n}_{\mathbf{r}+ae_x}^y \tilde{n}_{\mathbf{r}}^x \mathcal{S}_{\mathbf{r}+ae_x} \cos \Phi_{\mathbf{r}} \\ & \quad - \tilde{n}_{\mathbf{r}}^y \tilde{n}_{\mathbf{r}+ae_x}^x \mathcal{S}_{\mathbf{r}} \cos \Phi_{\mathbf{r}+ae_x} \} \\ & + D \sum_{\mathbf{r}} \tilde{n}_{\mathbf{r}}^y \tilde{n}_{\mathbf{r}+ae_y}^y \{ -\mathcal{C}_{\mathbf{r}+ae_y} \mathcal{S}_{\mathbf{r}} \sin \Phi_{\mathbf{r}+ae_y} + \mathcal{C}_{\mathbf{r}} \mathcal{S}_{\mathbf{r}+ae_y} \sin \Phi_{\mathbf{r}} \} + \{ \tilde{n}_{\mathbf{r}+ae_y}^y \tilde{n}_{\mathbf{r}}^x \mathcal{S}_{\mathbf{r}+ae_y} \sin \Phi_{\mathbf{r}} \\ & \quad - \tilde{n}_{\mathbf{r}}^y \tilde{n}_{\mathbf{r}+ae_y}^x \mathcal{S}_{\mathbf{r}} \sin \Phi_{\mathbf{r}+ae_y} \} \quad (4.2.3)\end{aligned}$$

where $\mathbf{r}' = \{\mathbf{r} + ae_x, \mathbf{r} + ae_y\}$ and correspond to lattice indices $\{i, j+1\}$ and $\{i+1, j\}$. In addition, $\mathcal{S}_{\mathbf{r}}$ and $\mathcal{C}_{\mathbf{r}}$ are shorthand for $\sin \Theta_{\mathbf{r}}$ and $\cos \Theta_{\mathbf{r}}$ respectively. As in previous simulations, we retain periodic boundary conditions.

Using this rather lengthy expression, the LLG equation for a *single* spin can be expressed in the following form:

$$i\omega \begin{bmatrix} 1 & \alpha \\ -\alpha & 1 \end{bmatrix} \begin{bmatrix} \tilde{n}_{\mathbf{r}}^x \\ \tilde{n}_{\mathbf{r}}^y \end{bmatrix} = \begin{bmatrix} H_{\mathbf{r}}^{eff,y} \\ -H_{\mathbf{r}}^{eff,x} \end{bmatrix} + \begin{bmatrix} 0 & -H_{\mathbf{r}}^{eff,z} \\ H_{\mathbf{r}}^{eff,z} & 0 \end{bmatrix} \begin{bmatrix} \tilde{n}_{\mathbf{r}}^x \\ \tilde{n}_{\mathbf{r}}^y \end{bmatrix} \quad (4.2.4)$$

where:

$$H_{\mathbf{r}}^{eff,x} = -\frac{\partial \mathcal{H}^{(2)}}{\partial \tilde{n}_{\mathbf{r}}^x} \quad (4.2.5)$$

$$H_{\mathbf{r}}^{eff,y} = -\frac{\partial \mathcal{H}^{(2)}}{\partial \tilde{n}_{\mathbf{r}}^y} \quad (4.2.6)$$

$$H_{\mathbf{r}}^{eff,z} = -\left. \frac{\partial \mathcal{H}^{(0)}}{\partial \tilde{n}_{\mathbf{r}}^z} \right|_{\tilde{n}_{\mathbf{r}}^z=1} \quad (4.2.7)$$

In order to recast Equation 4.2.4 in the form of a eigenvalue equation, we define the vector $\vec{\nu}$, which contains the perturbations to all N^2 spins in the lattice:

$$\vec{\nu} = [\tilde{n}_{1,1}^x, \tilde{n}_{1,2}^x, \dots, \tilde{n}_{N,N}^x, \tilde{n}_{1,1}^y, \tilde{n}_{1,2}^y, \dots, \tilde{n}_{N,N}^y]^T \quad (4.2.8)$$

With this, we obtain the complete eigenvalue problem:

$$i\omega(1 + \alpha^2)\vec{\nu} = \left(\begin{bmatrix} 1 & -\alpha \\ \alpha & 1 \end{bmatrix}_{\{i,j\}} \mathbf{H}^{eff} + \mathcal{H}_{\{i,j\}}^{eff,z} \begin{bmatrix} -\alpha & -1 \\ 1 & -\alpha \end{bmatrix}_{\{i,j\}} \right) \vec{\nu} \quad (4.2.9)$$

All matrices shown are $2N^2 \times 2N^2$ matrices. Subscripts $\{i,j\}$ imply that matrices act on the 2 dimensional subspace of $\vec{\nu}$ with lattice indices $\{i,j\}$. \mathbf{H}^{eff} is the matrix that calculates effective magnetic fields in Equations 4.2.5 and 4.2.6. From Equation 4.2.3, we can see that the $H_{\mathbf{r}}^{eff,x}$ and $H_{\mathbf{r}}^{eff,y}$ terms couple lattice site $\{i,j\}$ to neighbouring lattice sites. Therefore, \mathbf{H}^{eff} is has no diagonal elements. \mathbf{H}^{eff} was numerically constructed from the equilibrium skyrmion profile using the relaxation method described in Section 2.4.

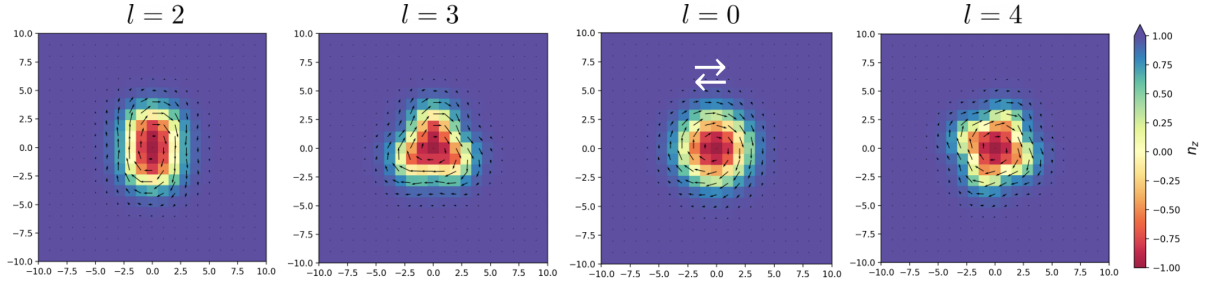
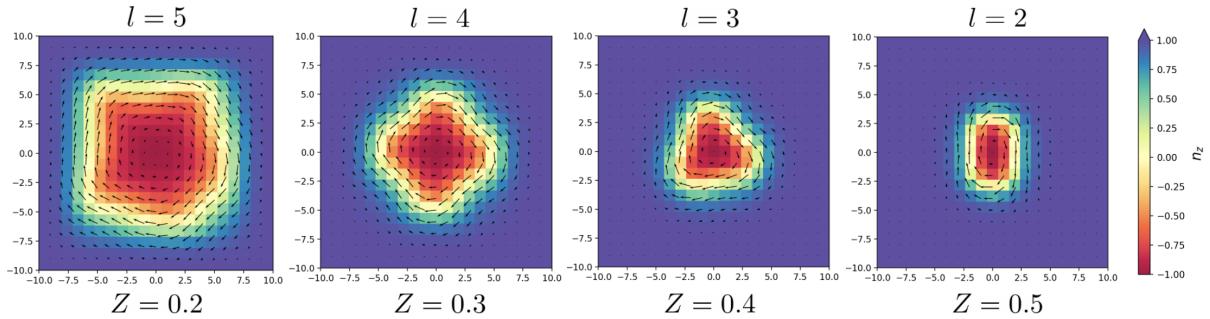
Upon diagonalising Equation 4.2.9, the eigen-vectors give the shape of the magnon modes, whilst the eigenvalues give the corresponding frequencies.

4.3 Bound Magnon modes

In order to maintain consistency with our simulations, we use $J = D = 1$ and $N = 21$. The eigenvectors of Equation 4.2.9 reveal that some of the fluctuation modes are well localised to the skyrmion profile. Much like the breathing and rotational modes studied in the previous chapter, these modes are collective excitations of the skyrmion spins. One can think of these excitations as bound magnon states in a pseudo-potential generated by the non-colinear spin texture of the skyrmion [39]. Figure 4.4 shows the first four, low frequency eigenmodes for $Z = 0.5$. Immediately, we can see that the low energy modes correspond to polygonal deformations of the skyrmion as reported in [6] and [21]. For $Z = 0.5$, the lowest lying mode corresponds to an elliptical distortion, which is described by polygonal number $l = 2$. Amongst the triangular $l = 3$ mode and the quadrupolar $l = 4$ mode, we also find a uniform translation mode described by $l = 0$, where the skyrmion wiggles horizontally. The time-dependence of the modes can be visualised by plotting:

$$\mathbf{n}(t) = \mathbf{n}_0 + \delta \mathbf{n} \sin(\omega_n t)$$

As shown in Figure 4.5, for lower magnetic fields, we find that the polygonal number of the lowest energy eigenmode increases.

Figure 4.4: Plots of the 4 lowest frequency magnon modes for $Z = 0.5$.Figure 4.5: Lowest energy eigenmode for $Z = 0.2, 0.3, 0.4, 0.5$.

This observation can be attributed to the skyrmion boundary becoming softer for lower magnetic fields, and therefore, supporting higher wave-number boundary harmonics with a comparably smaller energy penalty. In contrast, at larger fields the decay length to the ferromagnetic phase decreases (as discussed in Section 1.2.2), which means distortions of the skyrmion boundary would be energetically costly. The asymmetrical distortion of the pentagonal mode at $Z = 0.2$ arises from the imposed boundary conditions ($\Theta_{\text{boundary}} = 0$) when numerically solving for the skyrmion profile.

We also find that the spectrum is symmetric for positive and negative eigenenergies. That is, each eigenmode $\vec{\nu}_i$ is associated with frequencies:

$$\omega_i^\pm = \pm \operatorname{Re} \omega_i + \operatorname{Im} \omega_i$$

The sign of $\operatorname{Re} \omega_n$ is not so relevant since it simply amounts to the phase oscillating in the opposite direction. Therefore, we shall focus on the eigenvalues where $\operatorname{Re} \omega_n > 0$.

Figure 4.6 shows how the lowest 8 eigenfrequencies vary as the Zeeman coupling Z is swept through the range $0.3 < Z \leq 0.65$, for Gilbert damping $\alpha = 0$. We choose not to probe $Z < 0.3$ since the size of the skyrmion becomes comparable to the system size, leading to unwanted distortion effects. In order to accurately track the evolution of the eigenmodes, Z is increased in steps $\delta Z = 0.0035$. By noting the corresponding eigenmodes for certain reference values of Z , we are able to label eigenvalues by their polygonal number l . Whilst it appears that some of the eigenmodes seize to exist beyond a critical field, this is an artifact caused by only plotting the first 8 eigenmodes. In reality, the frequencies of these modes continue to increase as Z increases.

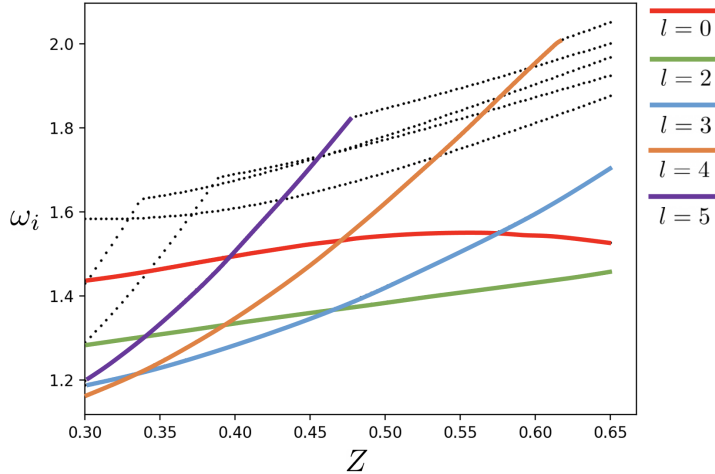


Figure 4.6: Lowest 8 Eigenfrequencies ω_i against Zeeman coupling Z . Eigenmodes are distinguished by their polygonal deformation number l . Black dots correspond to eigenfrequencies of higher order polygonal modes ($l \geq 6$) and continuum states.

Besides this detail, the spectra exhibits a few curious features. Notably, we find several level crossings corresponding to fields where two eigenmodes become degenerate. For instance, at $Z = 0.3$, the $l = 3$ mode has a lower energy than the $l = 2$ mode, whilst at $Z = 0.5$, the lowest energy mode is the elliptical mode. A similar level crossing has been reported in previous studies of skyrmion magnon modes [6][21]. However, for our system, these crossings occur more frequently. As Z increases, the frequencies of high- l eigenmodes increase more rapidly than those with low polygonal number. That is, $\delta\omega_i/\delta Z$ is greater for larger l , suggesting that high- l modes are more sensitive to small perturbations in the magnetic field. Only the $l = 0$ can be seen to lower in energy as Z approaches 0.6. The gapped $l = 0$ mode reflects the finite energy penalty associated with moving the skyrmion centre on a discrete lattice.

Importantly, our data shows that none of the eigenfrequencies drop to zero as Zeeman coupling is increased. This means the excitation energy $\Delta E \propto \hbar\omega_i$ is always finite. In our calculations, gapless magnon modes do not necessarily explain the elliptic / quadrupolar instabilities reported in this chapter. For the case of the elliptic instability, it is possible that the lowest lying eigenmode is gapped, and subsequently excited by the in-plane pulse. For the quadrupolar instability, the case for gapless magnon modes looks less convincing, since this instability occurs in the absence of any pulsed excitation. One could argue that the relaxation dynamics of the initial skyrmion excites the quadrupolar $l = 4$ mode. However, the difficulty with this statement is that the relaxation dynamics respect the azimuthal symmetry of the skyrmion profile, since it constitutes small amplitude radial oscillations and gradual changes in the radial twisting profile of the spins. Therefore, on symmetry grounds, we do not expect relaxation dynamics to give rise to the $l = 4$ distortion. Moreover, we did not see evidence of the $l = 3$ distortions for any value of Z . This is peculiar on energetic grounds, since one would expect the $l = 3$ mode to soften for Zeeman coupling between the elliptical and quadrupolar instability thresholds. Perhaps the most compelling argument against gapless magnon modes is that for finite Gilbert damping, $\text{Im } \omega_i > 0$. This means the eigenmode oscillations will be exponentially damped:

$$\delta n e^{i\omega_n t} \sim A e^{-\text{Im } \omega_n t} e^{i\text{Re } \omega_n t}$$

4.4 Energetic considerations

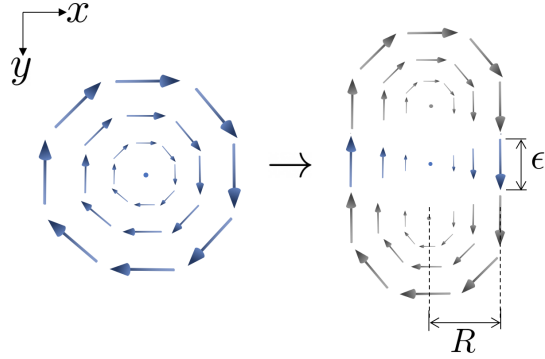


Figure 4.7: Schematic diagram of bi-meron perturbation.

In order to build some intuition for the formation of bi-merons, we now analyse a simplified picture of the elliptical instability. As shown in Figure 4.7, we model the elliptical distortion as the insertion of helix domain walls, with total thickness ϵ , between two half-skyrmions (merons). The total energy of the perturbed skyrmion is:

$$E = 2E_{halfsky} + E_{helix} \quad (4.4.1)$$

Clearly $2E_{halfsky} = E_{sky}$, therefore we are only concerned in calculating the energy shift E_{helix} induced by the spin-spiral. In order to achieve this, one must take the profile of the skyrmion into account, since this will determine the twisting of spins in the helical linkage. We use a simple ansatz:

$$\Theta(x) = \pi \left[1 + \tanh \left(\frac{x \ln \sqrt{3}}{R} \right) \right] \quad (4.4.2)$$

This ansatz has the property that as $x \rightarrow -\infty$, $\Theta(x) \rightarrow 0$ and $x \rightarrow \infty$, $\Theta \rightarrow 2\pi$. In addition, the scale factor $\ln \sqrt{3}/R$ was chosen such that the skyrmion radius R is given by the solution to $\Theta(x) = \pi/2$.

We now calculate the different contributions of the Hamiltonian (Equation 1.2.1) to E_{helix} . The helical spin-texture is given by:

$$\mathbf{n} = [0, -\sin \Theta(x), \cos \Theta(x)]^T \quad (4.4.3)$$

We obtain the total exchange energy E_{helix}^J :

$$E_{helix}^J = \frac{J}{2} \int_0^\epsilon dy \int_{-\infty}^{+\infty} dx \left(\frac{d\Theta}{dx} \right)^2 = \frac{2J\epsilon}{3} \cdot \frac{\pi^2 \ln \sqrt{3}}{R} \quad (4.4.4)$$

The DM contribution reads:

$$E_{helix}^D = -D\epsilon \int_{-\infty}^{+\infty} dx \frac{d\Theta}{dx} = -2D\pi\epsilon \quad (4.4.5)$$

Finally, the Zeeman contribution gives:

$$E_{helix}^Z = Z\epsilon \int_{-\infty}^{+\infty} dx (1 - \cos(\Theta)) \quad (4.4.6)$$

This term has no closed-form expression, since the integral is given in terms of cosine integral functions $\text{Ci}[x \pm \tanh(x \ln \sqrt{3}/R)]$. Instead, we can make progress by noticing that the integrand rapidly goes to zero for $x \rightarrow \pm\infty$, whilst $1 - \cos \Theta(x = 0) = 2$. Therefore, for small R , the integrand can be approximated by a top-hat function:

$$1 - \cos \Theta \approx \begin{cases} 2 & |x| \leq R \\ 0 & |x| > R \end{cases} \quad (4.4.7)$$

This is quite a naive approximation, but it is reasonable for skyrmions with small radii. With this, we get:

$$E_{\text{helix}}^Z \approx 4ZR\epsilon \quad (4.4.8)$$

Hence, our estimate for the energy of the helical linkage is:

$$E_{\text{helix}} \approx \epsilon \left(\frac{2J}{3} \cdot \frac{\pi^2 \ln \sqrt{3}}{R} + 4ZR - 2D\pi \right) \quad (4.4.9)$$

In order for this perturbation to constitute a local instability of the skyrmion, the expression in the brackets must turn negative. Therefore, one can estimate the critical Zeeman coupling Z_{crit} :

$$Z_{\text{crit}} \approx \frac{D\pi}{2R} - \frac{\pi^2 J \ln \sqrt{3}}{6R^2} \quad (4.4.10)$$

Visually, we estimate $R \approx 2$ from Figure 4.1. Substituting $D = J = 1$, as in our simulations, we obtain $Z_{\text{crit}} \approx 0.56$. Despite the crude approximation in Equation 4.4.7, this value is surprisingly close to our numerical upper-bound of $Z = 0.6$.

This calculation allows us to conclude that below $Z = 0.6$, the system energetically favours growth of the helical linkage. However, the skyrmion is prevented from breaking down into a helical stripe domain, since there is a larger energy penalty associated with removal of the meron caps. The competition between these two effects is responsible for the elliptical instability.

By definition, our naive model is unable to predict the lower bound of $Z = 0.5$, below which the quadrupolar deformation dominates. A possible explanation for the quadrupolar instability is that at sufficiently low fields, the single skyrmion is simply a metastable excitation in the ferromagnetic phase. The continuum theory suggests that for $Z \lesssim 0.8$ (Figure 1.3), the energy of a single skyrmion is negative, so the system favours the production of multiple skyrmionic textures. In this regard, for $Z \leq 0.3$ the quadrupolar instability facilitates the fragmentation of the skyrmion to form multiple bi-meron textures. However, as yet, it is unclear why a quadrupolar deformation, and not some other polygonal deformation, is the optimal manner to achieve such fragmentation.

4.5 Summary

In this chapter we have identified two geometric instabilities exhibited by the skyrmion. The first is an elliptical instability, triggered an in-plane magnetic field pulse for $0.5 \leq Z < 0.6$. The second is a spontaneous quadrupolar instability for $Z \leq 0.3$, where we observe a quadrupolar deformation propagate along the boundary of the skyrmion until it fragments into smaller, elongated skyrmions. The magnon spectrum was numerically

calculated, revealing that the lowest energy excitations are polygonal deformations. By plotting the eigenfrequencies against Zeeman coupling strength, we find that all of the magnon modes are gapped with a positive damping constant, reflecting their inability to explain such geometric instabilities in terms of gapless magnon modes. However, by considering the elliptical instability as two half-skyrmions connected by a domain wall, we shed light on the elliptical instability by analytically calculating the critical Zeeman coupling.

Chapter 5

Discussion & Outlook

5.1 Performance Issues and Optimisation

A key limiting factor throughout this project has been computational power. Our micro-magnetic simulation requires numerically solving the LLG equation for $3N^2$ spin components at each time-step. This leads to lengthy run-times even to obtain the simplest of results. The run-time is further increased when abrupt changes are made to the system, such as the application of magnetic pulses used in Chapter 3. Due to the large computational power needed to run the simulation, we limited the number of lattice points (N^2) in our system. For this reason, we could only simulate small skyrmions spanning approximately ten unit cells.

While developing the simulation, many calculations were completed using nested for loops. While this was useful for prototyping functions, processes involving nested loops are highly in-efficient. In order to reduce the run-time, many of the nested loops were vectorised, thus reducing the $\mathcal{O}(N^2)$ processes down to $\mathcal{O}(N)$.

The functions `H_matrix()` and `M_matrix()` (see Electronic Appendix A) were our main focus for vectorisation, since they are called at every time-step. Prior to vectorisation, these functions were calculating the elements of the $3N^2 \times 3N^2$ matrices one lattice site at a time. Once vectorised, we were able to compute the calculations for an entire lattice row at any one time. Since it was being called from `H_matrix()`, the effective magnetic field calculation also had to be vectorised. This was achieved by modifying our calculations to index the magnetisation arrays with vectors containing the lattice indices needed. The method of storing the effective magnetic field vectors was also altered, since we would now need to store the vectors for an entire row of lattice sites at one time, rather than individual sites. For a given row i , the effective field data was stored in the form:

$$\mathbf{H}_{eff}^i = \begin{bmatrix} H_{i,0}^x & H_{i,1}^x & H_{i,2}^x & \dots & H_{i,N}^x \\ H_{i,0}^y & H_{i,1}^y & H_{i,2}^y & \dots & H_{i,N}^y \\ H_{i,0}^z & H_{i,1}^z & H_{i,2}^z & \dots & H_{i,N}^z \end{bmatrix} \quad (5.1.1)$$

where each column contains the effective magnetic field vector $\mathbf{H}_{i,j}^{eff}$ for a site in that row.

Vectorising these functions shaved ~ 1 second from the run-time. Some time was spent optimising the simulation using Cython, a programming language that allows Python code to be compiled into C to gain the efficiency of the C programming language. We

were able to cythonize certain functions that were continuously looped over within our simulation. This resulted in a modest efficiency boost of 16%.

Toward the end of this project, we were fortunate enough to gain access to high-power computing facilities at the University. Running our code on this system helped shorten the run-time significantly, reducing it by around 60%. For this reason, we ran our most computationally intensive code, such as phase plots, on the high-powered system.

5.2 Theoretical Limitations

A shortcoming in this project's theoretical work is that we describe skyrmions in the continuum limit, whereas the skyrmions simulated in our thesis are in the opposite length regime. This disparity means the theoretical calculations have limited predictive power. Any theoretical arguments proposed in this paper can only serve to provide intuitions for trends observed in the numerical data.

To facilitate a small skyrmion within our limited lattice array, we used a value of $D/J = 1$ for the DM interaction strength. For this value of D/J , the spin-spiral wavelength only spans a few unit cells, thus allowing our single-skyrmion to be simulated within a 21×21 lattice without suffering boundary effects. It is important to note that such a large DM interaction strength is unrealistic, since the DM interaction in real materials is much weaker than the exchange interaction. Generally, the published research investigations on skyrmions used $D/J \ll 1$, allowing for bigger skyrmions to be stabilised within the larger systems being simulated. An extension to this project could numerically scrutinise our theoretical calculation. This would require further optimisation of the simulation code, or access to increased computing power.

5.3 Next Nearest Neighbour Interactions

In our simulation model, we consider only the interactions between nearest-neighbour (NN) lattice sites for the exchange and DM interactions. This was a deliberate choice made to reduce the computational intensity of the simulation. As a result of using a small system lattice array, the system dynamics would be significantly affected by including higher-order interaction terms in the Hamiltonian. Anisotropies induced by the discretization of the continuum model could be compensated for by introducing these higher-order NNN terms.

Magnetic frustration would arise within the system, arising from the competition between the two exchange interaction terms. The NNN exchange interaction Hamiltonian is given by:

$$\mathcal{H}'_{exch} = \sum_{\mathbf{r}} \sum_{j=\{x,y\}} J' \mathbf{n}_{\mathbf{r}} \cdot \mathbf{n}_{\mathbf{r}+2\hat{\mathbf{e}}_j} \quad (5.3.1)$$

where J' is the strength of the NNN exchange interaction [40]. How this additional term affects the system dynamics is determined by the sign of J' and the ratio of the two interaction strengths J'/J . For $J' > 0$, the interaction term is anti-ferromagnetic. In this

case, the window in which a skyrmion is stabilised by the DM interaction increases and then shrinks as the ratio J'/J is increased. The anti-ferromagnetic NNN interaction can also decrease the contribution of the exchange interaction, leading to the DM interaction providing a more significant contribution to the system dynamics. Alternatively, when the interaction is ferromagnetic for $J' < 0$, the stable skyrmion solution region shrinks as J'/J is increased [41].

The NNN contribution for the DM interaction can also be included in the form:

$$\mathcal{H}'_{DMI} = \sum_{\mathbf{r}} \sum_{j=\{x,y\}} D' \mathbf{n}_{\mathbf{r}} \times \mathbf{n}_{\mathbf{r}+2\hat{\mathbf{e}}_j} \cdot \hat{\mathbf{e}}_j \quad (5.3.2)$$

where D' is the DM interaction strength between NNN. These additional Hamiltonian terms describing the NNN interactions add higher-order contribution terms, thus providing a better approximation to the continuum model. This could be particularly useful in a small system such as the one used throughout this project, which already strays away from the continuum model due to a coarse lattice. The accuracy gained by using the NNN interactions however, will come at the cost of completing more computational processes.

5.4 Bi-meron wires

Throughout our investigations we have disregarded the physics of itinerant electrons, instead focusing on the magnetic dipole moments generated by electrons deep below the Fermi level. As such, we have treated these magnetic dipoles as semi-classical 3-vectors, since for typical skyrmion-hosting materials, the magnetic ions possess a spin quantum number (S) of order 10^1 . However, when one considers the Hund's coupling of free electrons to the skyrmionic spin-textures $\mathbf{n}(\mathbf{r})$, the free electron spins must be treated quantum mechanically since $S = 1/2$. This coupling is expressed as:

$$H_{Hund} = \mathcal{J} \hat{\boldsymbol{\sigma}} \cdot \mathbf{n}(\mathbf{r}) \quad (5.4.1)$$

where \mathcal{J} is the coupling constant and $\hat{\boldsymbol{\sigma}}$ is a 3-vector of Pauli matrices. Previous investigations have shown that this coupling gives rise to an emergent gauge field, which can be interpreted as a form of spin-orbit coupling [42][4][43]

For the reasons outlined above, we propose that the bi-merons of Chapter 4 could be promising candidates for experimental realisations of the Kitaev chain [44], when proximitised to an s-wave superconductor. Such a system is schematically illustrated in Figure 5.1. Previous studies have theoretically demonstrated that hybrid skyrmion-superconducting systems have the capability of inducing the topological superconductivity required to realise the Kitaev chain [45]. Notably, Güngörđü *et al.* have demonstrated that such a system can support localised Majorana zero-modes at the ends of an elongated skyrmion [46]. Whilst their elongated skyrmions were produced using a narrow confining geometry, our simulations demonstrate that below a critical magnetic field, skyrmions can spontaneously elongate, without the need for a specific confining geometry. An advantage of our system, is that the absence of any confining geometry would make it easier to perform unitary gate operations by moving superconducting vortices around the ends of the wire [47]. Future investigations could solve the Bogoliubov de Gennes Hamiltonian for free-electrons coupled to the bi-meron texture, and investigate the production of Majorana

zero modes in our system. Such an investigation could also research how the localisation of these modes (reflected in the probability density $|\Psi|^2$) varies for different micromagnetic parameters J , Z and D .

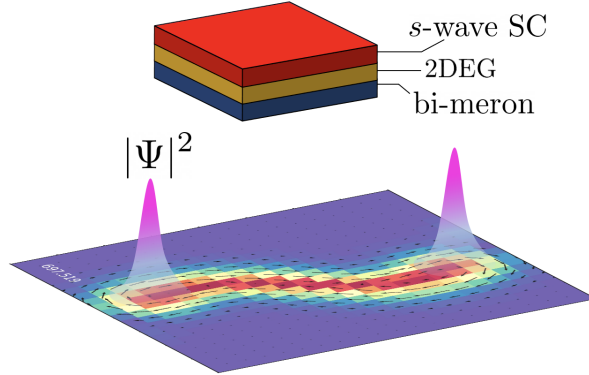


Figure 5.1: Proposal for hybrid skyrmiон-superconducting system that could exhibit topological superconductivity. By sandwiching a 2D electron gas (2DEG) between an s -wave superconductor (SC) and magnetic thin-film hosting a bi-meron, we predict localised Majorana zero-modes at the ends of the bi-meron given by peaks in the probability density $|\Psi|^2$.

Conclusion

In summary, we have developed a micro-magnetic simulation capable of modelling magnetic skyrmions, and used it to investigate the internal modes of a single-skyrmion. By applying an out-of-plane magnetic pulse to the system, we excited a breathing mode where the skyrmion radius oscillated in a damped harmonic manner. A single resonance peak, corresponding to the breathing mode, was observed in the absorption spectra of the system. The resonant frequency was seen to increase upon increasing the Zeeman coupling strength. This observation was corroborated using an argument based on scaling relations of the interactions present in the system. By applying an in-plane magnetic pulse, a counter-clockwise rotational mode of the skyrmion was excited. From the literature, we had expected to also observe a higher-energy clockwise mode, but this remained absent. Using a toy model, we proposed the possibility of negligible skyrmion mass term due to a large energy penalty associated with the in-plane magnetic spin fluctuations, stemming from the large value of the DM interaction strength used. This we believe, suppressed the clockwise rotational mode.

We also reported two geometric instabilities of the single-skyrmion. The first was an elliptical instability triggered by the in-plane magnetic pulse in the region $0.5 \leq Z < 0.6$. A spontaneous quadrupolar instability was also seen for $Z \leq 0.3$, which caused fragmentation of the skyrmion into smaller, elongated skyrmions. By numerically calculating the magnon spectrum, we found the lowest energy excitations are polygonal deformations. All of the magnon modes were found to be gapped, and so we were unable to explain the instabilities in terms of gapless magnon modes. By modelling the elliptical instability as two-half skyrmions connected by a domain wall, we analytically calculated the upper bound of the critical Zeeman coupling for the elliptical instability. In the final chapter, we discussed the theoretical limitations of our project associated with approximating the continuum model.

Our investigations demonstrate that the rigid-particle picture of magnetic skyrmions is insufficient when they are exposed to abrupt changes in the magnetic field. In these circumstances, one must account for the collective oscillations of the skyrmion spins. Furthermore, we have shown that for low magnetic fields, skyrmions do not even retain their circular symmetry, instead forming elongated bimeron composites. These considerations not only pose new puzzles regarding the experimental control and stabilisation of skyrmions, but also hint towards their novel applicability as deformable nano-wires.

Bibliography

- [1] Tom Lancaster. Skyrmions in magnetic materials. *Contemporary Physics*, 60(3):246–261, 2019.
- [2] Ian J. R. Aitchison. Tony skyrme and the origins of skyrmions, 2020.
- [3] THR Skyrme. A non-linear field theory. *Proc. Roy. Soc. (London) A*, 260, 1961.
- [4] Tomek Schulz, R Ritz, Andreas Bauer, Madhumita Halder, Martin Wagner, Chris Franz, Christian Pfleiderer, Karin Everschor, Markus Garst, and Achim Rosch. Emergent electrodynamics of skyrmions in a chiral magnet. *Nature Physics*, 8(4):301–304, 2012.
- [5] Kai Litzius, Ivan Lemesh, Benjamin Krüger, Pedram Bassirian, Lucas Caretta, Kornel Richter, Felix Büttner, Koji Sato, Oleg A Tretiakov, Johannes Förster, et al. Skyrmion hall effect revealed by direct time-resolved x-ray microscopy. *Nature Physics*, 13(2):170–175, 2017.
- [6] Shi-Zeng Lin, Cristian D Batista, and Avadh Saxena. Internal modes of a skyrmion in the ferromagnetic state of chiral magnets. *Physical Review B*, 89(2):024415, 2014.
- [7] Sebastian Mühlbauer, Benedikt Binz, F Jonietz, Christian Pfleiderer, Achim Rosch, Anja Neubauer, Robert Georgii, and Peter Böni. Skyrmion lattice in a chiral magnet. *Science*, 323(5916):915–919, 2009.
- [8] Shinichiro Seki, XZ Yu, S Ishiwata, and Yoshinori Tokura. Observation of skyrmions in a multiferroic material. *Science*, 336(6078):198–201, 2012.
- [9] Florian Jonietz, Sebastain Mühlbauer, Christian Pfleiderer, Andreas Neubauer, Wolfgang Münzer, Andreas Bauer, T Adams, Robert Georgii, Peter Böni, Rembert A Duine, et al. Spin transfer torques in mnsi at ultralow current densities. *Science*, 330(6011):1648–1651, 2010.
- [10] Masahito Mochizuki and Shinichiro Seki. Magnetoelectric resonances and predicted microwave diode effect of the skyrmion crystal in a multiferroic chiral-lattice magnet. *Physical Review B*, 87(13):134403, 2013.
- [11] Masahito Ikka, Akihito Takeuchi, and Masahito Mochizuki. Resonance modes and microwave-driven translational motion of a skyrmion crystal under an inclined magnetic field. *Physical Review B*, 98(18):184428, 2018.
- [12] Y Onose, Y Okamura, S Seki, S Ishiwata, and Y Tokura. Observation of magnetic excitations of skyrmion crystal in a helimagnetic insulator cu 2 oseo 3. *Physical review letters*, 109(3):037603, 2012.

- [13] Steven H Simon. *The Oxford solid state basics*. OUP Oxford, 2013.
- [14] Tôru Moriya. Anisotropic superexchange interaction and weak ferromagnetism. *Physical review*, 120(1):91, 1960.
- [15] Igor Dzyaloshinsky. A thermodynamic theory of “weak” ferromagnetism of antiferromagnetics. *Journal of Physics and Chemistry of Solids*, 4(4):241–255, 1958.
- [16] Utkan Güngörđü, Rabindra Nepal, Oleg A Tretiakov, Kirill Belashchenko, and Alexey A Kovalev. Stability of skyrmion lattices and symmetries of quasi-two-dimensional chiral magnets. *Physical Review B*, 93(6):064428, 2016.
- [17] Jung Hoon Han. *Skyrmions in Condensed Matter*, volume 278. Springer, 2017.
- [18] A Bogdanov and A Hubert. Thermodynamically stable magnetic vortex states in magnetic crystals. *Journal of magnetism and magnetic materials*, 138(3):255–269, 1994.
- [19] KF Riley, MP Hobson, and SJ Bence. Mathematical methods for physics and engineering, 1999.
- [20] JD Riley, DD Morrison, and JF Zancanaro. Multiple shooting methods for two-point boundary value problems, comm. *AMC*, 1(5):613–614, 1962.
- [21] Christoph Schütte and Markus Garst. Magnon-skyrmion scattering in chiral magnets. *Physical Review B*, 90(9):094423, 2014.
- [22] M Lakshmanan. The fascinating world of the landau–lifshitz–gilbert equation: an overview. *Philosophical Transactions of the Royal Society A: Mathematical, Physical and Engineering Sciences*, 369(1939):1280–1300, 2011.
- [23] Thomas L Gilbert. A phenomenological theory of damping in ferromagnetic materials. *IEEE transactions on magnetics*, 40(6):3443–3449, 2004.
- [24] OA Tretiakov, D Clarke, Gia-Wei Chern, Ya B Bazaliy, and O Tchernyshyov. Dynamics of domain walls in magnetic nanostrips. *Physical review letters*, 100(12):127204, 2008.
- [25] BF McKeever, DR Rodrigues, D Pinna, Ar Abanov, Jairo Sinova, and K Everschor-Sitte. Characterizing breathing dynamics of magnetic skyrmions and antiskyrmions within the hamiltonian formalism. *Physical Review B*, 99(5):054430, 2019.
- [26] XS Wang, HY Yuan, and XR Wang. A theory on skyrmion size. *Communications Physics*, 1(1):1–7, 2018.
- [27] Joo-Von Kim and Jeroen Mulders. On quantifying the topological charge in micromagnetics using a lattice-based approach. *IOP SciNotes*, 1(2):025211, 2020.
- [28] B Berg and Martin Lüscher. Definition and statistical distributions of a topological number in the lattice $O(3)$ σ -model. *Nuclear Physics B*, 190(2):412–424, 1981.
- [29] Masahito Mochizuki. Spin-wave modes and their intense excitation effects in skyrmion crystals. *Physical Review Letters*, 108(1).

- [30] Vitalii Kapitan, Egor Vasiliev, and Alexander Perzhu. Computer simulation of magnetic skyrmions. *Proceedings*, 46, 2020.
- [31] XZ Yu, Yoshinori Onose, Naoya Kanazawa, Joung Hwan Park, JH Han, Yoshio Matsui, Naoto Nagaosa, and Yoshinori Tokura. Real-space observation of a two-dimensional skyrmion crystal. *Nature*, 465(7300):901–904, 2010.
- [32] Daniel Capic, Dmitry A Garanin, and Eugene M Chudnovsky. Skyrmion–skyrmion interaction in a magnetic film. *Journal of Physics: Condensed Matter*, 32(41):415803, 2020.
- [33] Gen Tatara, Hiroshi Kohno, and Junya Shibata. Microscopic approach to current-driven domain wall dynamics. *Physics Reports*, 468(6):213–301, 2008.
- [34] Imam Makhfudz, Benjamin Krüger, and Oleg Tchernyshyov. Inertia and chiral edge modes of a skyrmion magnetic bubble. *Physical review letters*, 109(21):217201, 2012.
- [35] Börge Göbel, Ingrid Mertig, and Oleg A Tretiakov. Beyond skyrmions: Review and perspectives of alternative magnetic quasiparticles. *Physics Reports*, 2020.
- [36] Motohiko Ezawa. Compact merons and skyrmions in thin chiral magnetic films. *Physical Review B*, 83(10):100408, 2011.
- [37] Karin Everschor-Sitte, Jan Masell, Robert M Reeve, and Mathias Kläui. Perspective: Magnetic skyrmions—overview of recent progress in an active research field. *Journal of Applied Physics*, 124(24):240901, 2018.
- [38] GM Wysin and AR Völkel. Normal modes of vortices in easy-plane ferromagnets. *Physical Review B*, 52(10):7412, 1995.
- [39] Junichi Iwasaki, Aron J Beekman, and Naoto Nagaosa. Theory of magnon-skyrmion scattering in chiral magnets. *Physical Review B*, 89(6):064412, 2014.
- [40] Stefan Buhrandt and Lars Fritz. The skyrmion lattice phase in three dimensional chiral magnets from monte carlo simulations. *Physical Review B*, 88, 2013.
- [41] H. Y. Yuan, O. Gomonay, and Mathias Kläui. Skyrmions and multi-sublattice helical states in a frustrated chiral magnet. *Physical Review B*, 96, 2013.
- [42] Naoto Nagaosa and Yoshinori Tokura. Topological properties and dynamics of magnetic skyrmions. *Nature nanotechnology*, 8(12):899–911, 2013.
- [43] A Neubauer, C Pfleiderer, B Binz, A Rosch, R Ritz, PG Niklowitz, and P Böni. Topological hall effect in the a phase of mnsi. *Physical review letters*, 102(18):186602, 2009.
- [44] A Yu Kitaev. Unpaired majorana fermions in quantum wires. *Physics-Uspekhi*, 44(10S):131, 2001.
- [45] Maxime Garnier, Andrej Mesaros, and Pascal Simon. Topological superconductivity with deformable magnetic skyrmions. *Communications Physics*, 2(1):1–8, 2019.

- [46] Utkan Güngörđü, Shane Sandhoefner, and Alexey A Kovalev. Stabilization and control of majorana bound states with elongated skyrmions. *Physical Review B*, 97(11):115136, 2018.
- [47] Sankar Das Sarma, Michael Freedman, and Chetan Nayak. Majorana zero modes and topological quantum computation. *npj Quantum Information*, 1(1):1–13, 2015.